IS-T-256

AMES LABORATORY

Iowa State University

Ames, Iowa

AEC Contract No. W-7405-eng-82

THERMAL CONDUCTIVITY AND LORENZ FUNCTION OF GADOLINIUM, TERBIUM, AND HOLMIUM SINGLE CRYSTALS

by

William Joel Nellis

Ph.D. Thesis, November 1968

LEGAL NOTICE

This report was prepared as an account of Government sponsored work. Neither the United States, nor the Commission, nor any person acting on behalf of the Commission:

A. Makes any warranty or representation, expressed or implied, with respect to the accuracy, completeness, or usefulness of the information contained in this report, or that the use of any information, apparatus, method, or process disclosed in this report may not infringe privately owned rights; or

B. Assumes any liabilities with respect to the use of, or for damages resulting from the use of any information, apparatus, method, or process disclosed in this report.

As used in the above, "person acting on behalf of the Commission" includes any employee or contractor of the Commission, or employee of such contractor, to the extent that such employee or contractor of the Commission, or employee of such contractor prepares, disseminates, or provides access to, any information pursuant to his employment or contract with the Commission, or his employment with such contractor.

THERMAL CONDUCTIVITY AND LORENZ FUNCTION OF GADOLINIUM, TERBIUM, AND HOLMIUM SINGLE CRYSTALS

by

William Joel Nellis

A Dissertation Submitted to the

Graduate Faculty in Partial Fulfillment of

The Requirements for the Degree of

DOCTOR OF PHILOSOPHY

Major Subject: Physics

Approved:

Sam Legvold

In Charge of Major Work

Head of Major Department

Dean of Graduate College

Iowa State University
Of Science and Technology
Ames, Iowa

November 1968

TABLE OF CONTENTS

THERMAL CONDUCTIVITY AND LORENZ FUNCTION OF GADOLINIUM, TERBIUM, AND HOLMIUM SINGLE CRYSTALS*

William Joel Nellis

ABSTRACT

The thermal conductivity of gadolinium, terbium, and holmium single crystals has been measured as a function of temperature from 5 to 300°K. The steady state heat flow method was used. For each element measurements were taken in the $[11\bar{2}0]$ (a-axis) and in the [0001] (c-axis) directions of the hexagonal close-packed crystal structure. Electrical resistivity measurements were made on the same samples to obtain Lorenz functions.

The a-axis conductivity of gadolinium shows a sharp change of slope at 294°K. The c-axis conductivity has a minimum at 275°K and goes smoothly through the Curie temperature, 293°K. The a-axis conductivity of terbium shows little indication of the Curie point at 221°K and manifests a change of slope at 231°K. The c-axis conductivity is essentially constant from 222°K to 230°K, the Neel point, at which temperature a change of slope occurs. In holmium the conductivities of both axes show slight decreases at 20°K, the Curie point. The a-axis conductivity has a minimum at 131°K, the Neel point. The c-axis conductivity increases below the Neel point and has a change of slope at 132°K.

Anomalies near magnetic transition temperatures are interpreted in terms of magnetic superzone energy gaps and spin disorder scattering. High temperature anisotropy is interpreted in terms of Fermi surface anisotropy. Lorenz numbers anomalously large relative to L_o suggest that phonons and magnons can carry heat in addition to electrons.

*USAEC Report IS-T-256. This work was performed under contract W-7405-eng-82 with the Atomic Energy Commission.

I. INTRODUCTION

The transport properties of the rare earth series of elements present to the experimenter an unusually interesting field of investigation. Unique among the other materials in the periodic table, the rare earth metals possess a wide variety of magnetic structures. Above room temperature nearly all of these elements are paramagnetic. However, below room temperature some rare earth elements still do not order magnetically, while others may order in up to three distinct magnetic structures. The affect of this magnetic ordering on the transport properties of these materials is sizeable. The purpose of this investigation is to add to our knowledge of these properties by determining the thermal conductivities of gadolinium, terbium, and holmium.

The rare earth, or lanthanide, series of elements runs from lanthanum, atomic number 57, to lutetium, atomic number 71. For the most part the rare earths have the following outer electron configuration:

$$(4f)^n(5s)^2(5p)^6(5d)^1(6s)^2 \quad ,$$

where n ranges from zero to fourteen across the series. The 5d and 6s electrons are the valence electrons, and because this valence structure is essentially common to all these elements they were originally difficult to separate. The most stable chemical structures are empty, half filled, and full 4f shells. Consequently, exceptions to the $(5d)^1(6s)^2$ valence structure arise when cerium and terbium, under certain rare circumstances, give up a 4f electron to the 5d shell to produce an empty and half filled 4f shell, respectively, and when europium and ytterbium shift a 5d electron to the 4f shell to produce a half filled and full 4f shell, respectively.

Aside from these exceptions the rare earths are trivalent and crystallize in the hexagonal close-packed structure.

The magnetic properties of the rare earths are due to the extent to which the 4f shell is filled and to the manner in which the 4f electrons interact. Magnetic ordering is an indirect process since the direct overlap integrals between 4f electrons on different sites are negligible. Rather, the 4f electrons on different atomic sites sense each other through the conduction electrons (1). In zero magnetic field this indirect exchange interaction can be expressed by the Heisenberg Hamiltonian

$$\mathcal{H} = -2 \sum_{i,j} V(\underline{R}_i - \underline{R}_j)(g-1)^2 \underline{J}_i \cdot \underline{J}_j \quad , \tag{1.1}$$

where $\underline{R}_i$ is the position of the ith ion with total angular momentum $\underline{J}_i$, g is the Lande g-factor, and V is the exchange integral.

On the other hand the anomalous transport properties of the rare earths are due to the direct exchange interaction between the conduction electrons and the 4f electrons (2). This exchange interaction can be expressed by the Heisenberg Hamiltonian

$$\mathcal{H} = N^{-1} \sum_{n=1}^{N} V_d \, (\underline{r} - \underline{R}_n)(g-1) \underline{J}_n \cdot \underline{\sigma} \quad , \tag{1.2}$$

where N is the number of ions, V_d is the exchange integral, $\underline{r}$ is the position vector of the conduction electron, $\underline{R}_n$ is the position of the nth ion, g is the Lande g-factor, $\underline{J}_n$ is the total angular momentum of the nth ion, and $\underline{\sigma}$ is the spin angular momentum of the conduction electron.

Band structure and Fermi surface calculations on gadolinium (3,4), terbium*, dysprosium (4), holmium (5), erbium (4), thulium (6), lutetium (4),

*A. R. Mackintosh, Physics Department, Technical University, Lundtofte, Lyngby, Denmark. Energy bands of terbium. Private communication. ca. 1968.

scandium (7), and yttrium (8) have shown the electronic structure of the rare earths to be extremely anisotropic. Scandium and yttrium are trivalent, hexagonal metals whose band structures are very similar to those of the rare earths. This anisotropy provides the motivation for using single crystals in these investigations.

Extensive work on the transport and magnetic properties of some rare earth single crystals has been done. Table 1 indicates the experimenters who performed the work on seven of the heavy rare earths and yttrium. Much less single crystal work has been done on the light rare earths. Numerous other investigations of the transport and magnetic properties of polycrystalline rare earths have also been carried out.

Table 1. References to experimental work performed on heavy rare earth and yttrium single crystals.

	Electrical Resistivity	Thermal Conductivity	Seebeck Coefficient	Hall Effect	Magnetic Moment
Gd	Nigh(9) Nellis	Nellis	Sill(16)	Lee(18)	Nigh(9)
Tb	Hegland(10) Nellis	Nellis	Sill(16)	------	Hegland(10)
Dy	Hall(11) Boys(12)	Boys(12)	Sill(16)	Rhyne(19)	Behrendt(20)
Ho	Strandburg(13) Nellis	Nellis	Sill(16)	------	Strandburg(13)
Er	Green(14) Boys(12)	Boys(12)	Sill(16)	------	Green(14)
Tm	Edwards(15)	Edwards(15)	Edwards(15)	------	Richards(21)
Lu	Boys(12)	Boys(12)	Edwards(17)	Lee(18)	------
Y	Hall(11)	------	Sill(16)	Lee(18)	------

Boys (12) measured the first thermal conductivities of rare earth single crystals. He used basal plane and c-axis samples of dysprosium,

erbium, and lutetium over the temperature range 5°-$300^{o}K$. He found pronounced anisotropy between the two axes of the same metal and manifestations of magnetic ordering in dysprosium and erbium. The room temperature values of the six samples varied from 0.10 to 0.23 watt/cm-^{o}K. Edwards (15) also found pronounced anisotropy and evidence for magnetic ordering in thulium. The room temperature values of his basal plane and c-axis samples were 0.143 and 0.241 watt/cm-^{o}K, respectively. Boys and Edwards both tabulated the Lorenz function

$$L = \frac{K}{T} \rho \quad , \tag{1.3}$$

where K is the thermal conductivity and ρ is the electrical resistivity at the temperature T. L_o is the theoretical value for pure electronic conduction and is given by

$$L_o = \frac{\pi^2}{3} \left(\frac{k}{e}\right)^2 = 2.45 \times 10^{-8} \text{ watt-ohm-cm/}^{o}K^2 \quad , \tag{1.4}$$

where k is Boltzmann's constant and e is the electronic charge. With the exception of the lutetium c-axis sample the Lorenz functions of all these samples were significantly larger than L_o.

The earliest work of polycrystalline rare earth thermal conductivity is that of Legvold and Spedding* in 1954 (22). They reported on eight rare earths and expected their results to be accurate to within 10%. The thermal conductivity of gadolinium at $28^{o}C \pm 2^{o}$ was stated to be 0.0880 watt/cm-^{o}K.

Arajs and Colvin in 1964 reported the thermal conductivity of polycrystalline gadolinium (23), terbium (24), and dysprosium (25), over the

*Sam Legvold, Physics Department, Iowa State University, Ames, Iowa. This work was done by John E. Cranch and his results appeared in an administrative report of Legvold and Spedding. Private Communication. 1968.

temperature range 5°-300°K. They found anomalous behavior near the Curie point in gadolinium and near the Néel point in terbium and dysprosium. Below these ordering temperatures they found the thermal conductivity to be essentially constant, while above these ordering temperatures the conductivity increased monotonically. In addition, the conductivity dropped sharply at the ferromagnetic-antiferromagnetic transition temperature in dysprosium. The Lorenz functions of all three elements were anomalously large relative to L_o over the whole temperature range. They interpreted this fact to be an indication of phonon and/or magnon heat conduction. Their observed room temperature values for gadolimium and terbium were both about 0.14 watt/cm-^{o}K.

Arajs and Dunmyre in 1965 reported the thermal conductivity of polycrystalline erbium over the temperature range 5°-300°K (26). Their results again showed a drop in the conductivity near the ferromagnetic-antiferromagnetic transition temperature and a monotonic increase above the ordering temperature.

Powell and Jolliffe in 1965 reported the thermal conductivities of eight rare earths near room temperature (27). At 18°C they found the thermal conductivities of gadolinium, terbium, and holmium to be 0.091, 0.103, 0.106 watt/cm-^{o}K, respectively.

Aliev and Volkenshtein in 1966 reported the thermal conductivity of polycrystalline gadolinium, terbium, holmium, erbium, thulium, ytterbium, and lutetium over the temperature range 2°-100°K (28,29,30). All these elements showed characteristic peaks near 20°K, as did the work of Arajs and Colvin and of Arajs and Dunmyre. Aliev and Volkenshtein also observed a kink in the conductivity of erbium at the ferromagnetic-antiferromagnetic

transition temperature and a rise in the conductivity above the ordering temperature. They differed most from the results of Arajs and his co-workers on terbium by obtaining much lower values above $40^{o}K$ and by finding a minimum at $5^{o}K$, which they attributed to impurities. The Lorenz functions of all their samples at $4.2^{o}K$ were anomalously large relative to L_o.

Jolliffe et al. in 1966 reported more room temperature thermal conductivities (31). Their results for gadolinium, terbium, and holmium were the same as those reported earlier by Powell and Joliffe.

Karagyozyan and Rao have investigated the thermal conductivity of gadolinium, terbium, and dysprosium in the temperature range 1°-$4^{o}K$ (32,33, 34). All three elements differ from the behavior one would expect at these temperatures. Their results are attributed to oxide impurities.

Nikolskii and Eremenko have reported the thermal conductivity of polycrystalline erbium in a magnetic field over the temperature range 20°-$100^{o}K$ (35). They conclude that their measurements are "direct evidence of the importance of magnon contributions to the total heat flow."

Summarizing experiments to date on the thermal conductivity of rare earth metals one can say the following:

1. The rare earths are poor thermal conductors relative to other metals. Copper and silver, for example, have room temperature thermal conductivities of about 4 watt/cm-^{o}K, while the conductivities of the rare earths at this temperature are in the range 0.1-0.25 watt/cm-^{o}K.

2. The thermal conductivity is very sensitive to magnetic ordering, especially in single crystals.

3. The thermal conductivity is very anisotropic.

4. Reported Lorenz functions are almost always anomalously large relative to L_o.

II. REVIEW OF THEORY

A. Formal Transport Theory

Thermal conductivity is a measure of the ability of a material to transport energy or heat. Mathematically, the thermal conductivity, K, is the proportionality factor relating the heat flow per unit time per unit area, $\underline{\dot{Q}}$, in the presence of a temperature gradient $\underline{\nabla}T$; i.e.,

$$\underline{\dot{Q}} = -K\underline{\nabla}T \quad . \tag{2.1}$$

The minus sign expresses the fundamental fact that heat flows from a region of higher temperature to a region of lower temperature.

In a solid metal there are three heat carriers: conduction electrons, lattice vibrations or phonons, and, in magnetic materials, spin waves or magnons. The total thermal conductivity is the sum:

$$K = K_e + K_g + K_m \quad , \tag{2.2}$$

where K is the total thermal conductivity and K_e, K_g, and K_m are the thermal conductivities of the electrons, phonons, and magnons, respectively. Review articles by Klemens (36) and by Mendelssohn and Rosenberg (37) summarize a great deal of experimental and theoretical work on non-magnetic solids.

The thermal resistivity of a given carrier is determined by the way in which the various scattering mechanisms impede the flow of that carrier. The assumption is usually made that the various scattering mechanisms are independent, and thus the contribution of each to the thermal resistivity can be added algebraically. Proceeding as in the case of Matthiessen's rule for electrical resistivity one can then write:

$$W_e = \sum_i W_e^i = 1/K_e \quad , \tag{2.3a}$$

$$W_g = \sum_i W_g^i = 1/K_g \quad , \tag{2.3b}$$

$$W_m = \sum_i W_m^i = 1/K_m \quad , \tag{2.3c}$$

where W_e^i, for example, is the thermal resistance for electrons being scattered by the ith scattering mechanism. Possible scattering mechanisms are electrons, phonons, magnons, impurities, and boundaries. The g and m refer to phonons and magnons, respectively.

There are two basic approaches to formal transport theory, the kinetic method and the Boltzmann equation. Before proceeding farther, however, it seems appropriate to point out a basic fact of all transport theories. Transport coefficients have not as yet been calculated exactly. Existing theories have, however, often contributed correct temperature dependences and orders of magnitude.

The simple kinetic approach yields

$$K = (1/3)Cv\,\Lambda \quad , \tag{2.4}$$

where C is the total specific heat of the carrier system, v is the carrier velocity, and Λ is the mean free path between collisions. This result is useful for determining temperature dependences.

The Boltzmann equation approach seeks to find a distribution function $f_{\underline{k}}(\underline{r})$ which is the number of carriers in the state $\underline{k}$ in the region near $\underline{r}$. Given this function, for the case of electrons the electrical current density, $\underline{J}$, and the energy current density, $\underline{U}$, are then calculated from

$$\underline{J} = \int e\underline{v}_{\underline{k}} f_{\underline{k}} d\underline{k} \tag{2.5a}$$

and

$$\underline{U} = \int (E_{\underline{k}} - \zeta)\, \underline{v}_{\underline{k}} f_{\underline{k}} d\underline{k} \quad , \tag{2.5b}$$

where e is the electronic charge, $v_{\underline{k}}$ and $E_{\underline{k}}$ are the velocity and energy of the electron, respectively, ζ is the free energy, and the integrals are over all occupied $\underline{k}$ states.

The distribution function is calculated from the steady state Boltzmann equation

$$\dot{f}_{\underline{k}} = \dot{f}_{\underline{k}}]_{diff} + \dot{f}_{\underline{k}}]_{field} + \dot{f}_{\underline{k}}]_{coll} = 0 \quad , \tag{2.6}$$

where the three bracketed terms are the time rate of change of the distribution function due to diffusion, external fields, and collisions, respectively.

In the relaxation time approximation

$$\dot{f}_{\underline{k}}]_{coll} = (f_{\underline{k}} - f^{o}_{\underline{k}})/\tau \tag{2.7}$$

where $f^{o}_{\underline{k}}$ is the equilibrium Fermi distribution and τ is the relaxation time. In this case Ziman (38, p.383) shows that

$$f_{\underline{k}} = f^{o}_{\underline{k}} - \tau(k)\underline{V}_{\underline{k}} \cdot [- \frac{E_{\underline{k}} - \zeta}{T} \frac{\partial f^{o}_{\underline{k}}}{\partial E_{\underline{k}}} \underline{\nabla} T + e \frac{\partial f^{o}_{\underline{k}}}{\partial E_{\underline{k}}} (\underline{E} - \frac{1}{e} \underline{\nabla} \zeta)] \quad , \tag{2.8}$$

where T is the absolute temperature and $\underline{E}$ is the external electric field.

Using this distribution function in the transport integrals, Equations 2.5, one obtains

$$\sigma_{ij} = \frac{e^2 \tau}{4\pi^3 \hbar} \int_{E_F} V_i dS_j \quad , \tag{2.9a}$$

$$K_{ij} = \frac{\pi^2}{3} (\frac{k}{e})^2 T\sigma_{ij} \quad , \tag{2.9b}$$

where σ_{ij} is the electrical conductivity ($J_i = \sigma_{ij} E_j$), dS_j is the component

of an elemental area of the Fermi surface, $d\underline{S}$, in the jth direction, and the integral is over the Fermi surface.

Equation 2.9b can be written as

$$L_o = \frac{K_{ij}\sigma_{ij}}{T} = \frac{\pi^2}{3}\left(\frac{k}{e}\right)^2 \quad . \tag{2.10}$$

L_o is the theoretical Lorenz number for electronic conduction and Equation 2.10 is known as the Wiedemann-Franz law. This law in reality holds for many pure metals when the scattering is elastic; i.e., at temperatures much lower than the Debye temperature of the material and at temperatures greater than the Debye temperature.

B. Electronic Conduction

Attention will now be turned to temperature dependences of thermal conductivity. The Wiedemann-Franz law holds at low and high temperatures. At low temperatures, in the residual resistance region, the resistivity is constant. Therefore,

$$1/W_e^i = \beta T \quad , \qquad (T \ll \theta_D) \tag{2.11}$$

where ideally $\beta = L_o/\rho_o$, θ_D is the Debye temperature, ρ_o is the residual resistance, and the superscript i denotes impurity scattering. The kinetic result (Equation 2.4) yields the same temperature dependence, since in this region the velocity and mean free path of the electron are assumed constant, while the specific heat of the electrons is proportional to T.

At high temperatures the resistivity is proportional to T, so that

$$1/W_e^g \sim \text{constant}, \qquad (T > \theta_D) \quad . \tag{2.12}$$

This last result is shown more rigorously by Ziman (38, p.389), who considers the electron-phonon interaction in some detail. At intermediate

temperatures and from these same considerations, Ziman shows that

$$W_e^g \sim T^2 \quad , \qquad (T < \theta_D) \quad . \tag{2.13}$$

Therefore, at low temperatures ($T \simeq \theta_D/10$), 2.3a, 2.11, and 2.13 yield

$$W_e = A/T + BT^2 = 1/K_e \quad . \tag{2.14}$$

Equation 2.14 describes the typical behavior of the thermal conductivity of pure metals: a peak at about $\theta_D/10$, a sharp decrease below $\theta_D/10$, and a gradual decrease above. Lutetium obeys this temperature dependence below about 16^oK quite well (12).

Figure 1 illustrates the behavior of K_e, as described above, and also the behavior of the Lorenz function of a pure metal. Note that L is nearly L_o at high and low temperatures. The dip in L at intermediate temperatures is interpreted to mean that inelastic scattering affects thermal conduction more drastically than electrical conduction. At these lower temperatures only the longer wavelength phonons are excited and the electrons are scattered through rather small angles. These collisions affect the transport of charge relatively little, but the electron can change its energy by about kT, which is enough to convert a "hot" electron to a "cold" one.

Ziman (38) predicts that at low temperatures electron-electron scattering should cause a thermal resistivity term $W_e^e \sim T^2$. Schriempf (39) recently observed such a T^2 contribution to the thermal resistivity of palladium, a transition metal.

Electrons are also scattered by magnetic moments in magnetic metals. Above the ordering temperature of these metals, there is a spin disorder contribution, ρ_s, to the resistivity. Dekker (40) used the Hamiltonian of Equation 1.2 and a spherical Fermi surface to show that for the rare earths

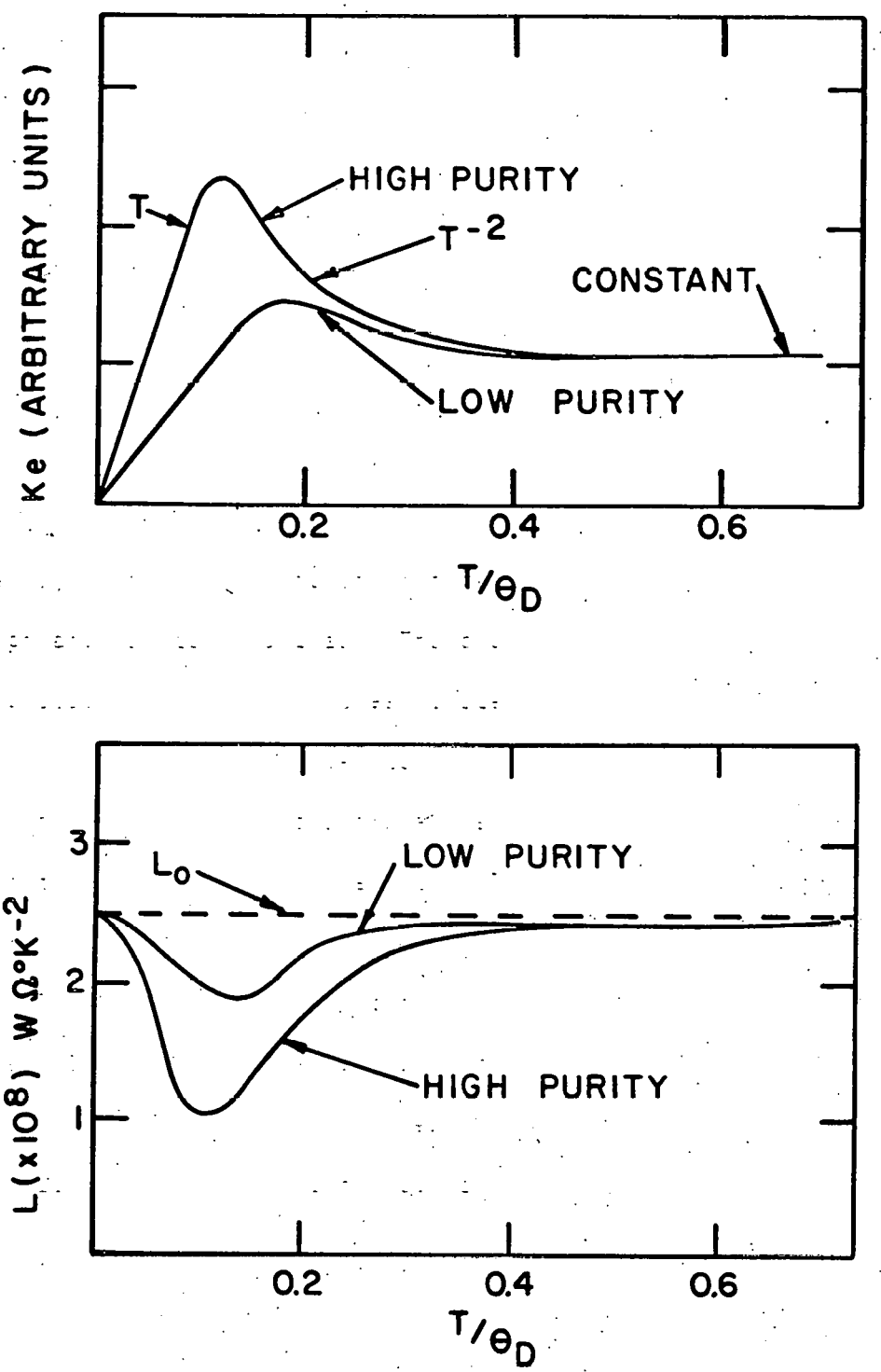

Figure 1. K_e and L for a pure metal in which impurities and phonons are the dominant scattering mechanisms

$$\rho_s = (3\pi Nm/2\hbar e^2 E_F) V_d^2 (g-1)^2 J(J+1) \quad , \tag{2.15}$$

where N is the number of atoms, m is the electron mass, and E_F is the Fermi energy. ρ_s is temperature independent. Since conduction electrons are scattered elastically by paramagnetic moments, the Wiedemann-Franz law yields

$$W_e^m \sim 1/T \quad , \qquad T > T_o \quad , \tag{2.16}$$

where m denotes magnetic scattering and T_o is the ordering temperature.

Liu and Siano (41) have investigated electron scattering in a Heisenberg ferromagnet. Their calculation showed a peak in W_e^m around the Curie point and they predict a dip in the total thermal conductivity near this temperature. This dip is clearly seen in the gadolinium a-axis sample used in this investigation. The c-axis sample, however, shows a gradual transition in the thermal conductivity and in the electrical resistivity as well.

The antiferromagnetic structures in the rare earths can introduce additional planes of energy discontinuity in the electronic structure. These superzone boundaries arise from the periodic arrangement of magnetic moments in a way similar to that in which Brillouin zone boundaries are caused by the periodic arrangement of atoms. Introduction of these superzones alters the Fermi surface and thus alters the conductivity integrals of Equations 2.9.

C. Phonon Conduction

Phonons can conduct heat in a metal. The total lattice thermal resistivity is

$$W_g = W_g^B + W_g^e + W_g^i + W_g^g + W_g^m \quad . \tag{2.17}$$

These terms represent phonon scattering by boundaries, electrons, impurities, phonons, and magnons, respectively.

At high temperatures the specific heat of a solid is constant. Phonons are scattered at a rate depending on the square of the amplitude of fluctuation of the ions, which is proportional to the temperature. Thus $\Lambda \sim 1/T$ and by Equation 2.4

$$W_g^g \sim T \quad , \qquad (T > \theta_D) \quad . \tag{2.18}$$

This argument is the classical one. Ziman (38, p. 289) obtains the same result by considering the phonon-phonon interaction in some detail and by calculating the Umklapp thermal resistivity. Phonon-phonon interactions can be described by

$$\underline{q} + \underline{q}' = \underline{q}'' + \underline{\tau} \quad , \tag{2.19a}$$

$$h\nu + h\nu' = h\nu'' \quad , \tag{2.19b}$$

where $\underline{q}$ and $\underline{q}'$ are the wave vectors of incident phonons, $\underline{q}''$ is the wave vector of the final phonon, $\underline{\tau}$ is a reciprocal lattice vector, ν and ν' are the frequencies of the incident phonons, and ν'' is the frequency of the final phonon. Normal processes are defined as those for which $\underline{\tau} = 0$; while in Umklapp processes $\underline{\tau} \neq 0$. Normal processes do not contribute to the thermal resistivity. As Peierls (42) pointed out, normal processes merely distribute the energy into different phonon modes. They do not affect the net flow of energy.

At low temperatures the specific heat of the phonon is proportional to

T^3 and the mean free path is of the order of the sample dimensions. Thus, in the boundary scattering region, by Equation 2.4

$$W_g^B \sim T^{-3} \quad . \tag{2.20}$$

As the temperature is increased and phonons can be scattered by electrons, Ziman shows that (38, p.322)

$$W_g^e \sim T^{-2} \quad , \tag{2.21}$$

assuming that the resistivity is proportional to T^5.

The effect of phonon-impurity scattering on the thermal conductivity depends on the type of impurity. Qualitatively, an increase in impurity lowers the peak in the lattice thermal conductivity.

Figure 2 illustrates the scattering mechanisms limiting the lattice component of the thermal conductivity of a non-magnetic metal.

The phonon-magnon interaction and its affect on the thermal conductivity has been considered for certain cases. Kawasaki (43) and Stern (44) were able to explain a dip in the thermal conductivity of CoF_2 at its Neel point, 38^oK. CoF_2 is an antiferromagnetic insulator. Kawasaki showed that the heat conducted by the spin system was negligible near the transition point.

D. Magnon Conduction

Most investigations of magnon conduction, both experimental and theoretical, have dealt with magnetic insulators. Sato (45) calculated that the magnon thermal conductivity in a ferromagnetic insulator is proportional to T^2 in the low temperature, boundary scattering region. Douthett and Friedberg also showed that in ferrite single crystals in zero magnetic

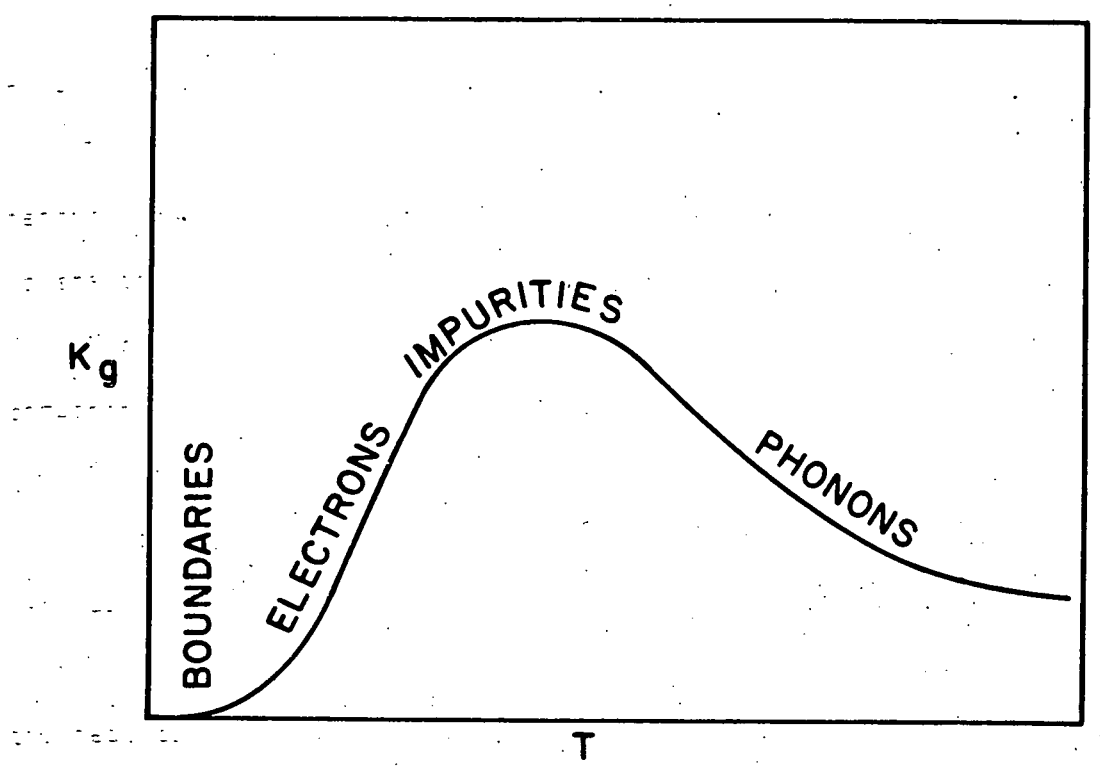

Figure 2. K_g for a metal. The dominant scattering mechanisms limiting K_g in the various temperature ranges are indicated

field the magnon thermal conductivity would have a quadratic temperature dependence (46). They assumed that only boundary scattering was important and that the magnon dispersion relation was quadratic in magnon wave vector. A T^2 contribution to the thermal conductivity in yttrium iron garnet was observed by Lüthi (47) and by Douglass (48). McCollum et al. found a similar contribution in the low temperature thermal conductivity of EuS (49). Bhandari and Verma (50) considered magnon-phonon interactions in yttrium iron garnet and using Douglass' data concluded that at $0.5^{\circ}K$ the magnon contribution could be as high as 46% of the thermal conductivity, but that the phonon conductivity rapidly dominates as the temperature is raised.

III. EXPERIMENTAL PROCEDURE

A. Sample Preparation

The rare earth metal used in this investigation was prepared at the Ames Laboratory. Each metal is separated from the other rare earths by an ion exchange process (51). Purification is accomplished by reduction from the fluoride, followed by distillation.

The single crystals were grown by the strain-anneal technique described by Nigh (52). The metal is strained by arc-melting and allowing it to freeze on a cold copper hearth. The metal is then hung in the furnace of Figure 3 and annealed. The terbium button and the button from which the holmium a-axis I sample was cut were sealed in tantalum crucibles as indicated in the figure. The gadolinium and holmium II buttons were not.

The crystals were aligned by Laue back-reflection of X-rays and cut by means of a spark erosion apparatus. Samples were cut in the form of rectangular parallelepipeds. All samples were aligned with their length along the $[11\bar{2}0]$ (a-axis) direction or along the [0001] (c-axis) direction.

The samples were mechanically polished with emery paper to achieve uniform cross section and length. They were then etched and electropolished so that indium solder would adhere to their surface. Sample dimensions were measured with a Brown and Sharpe micrometer to the nearest 0.001 inch. The sample ends were tinned with pure indium with an ultrasonic soldering iron and the sample was mounted in the sample holder.

Both terbium samples and both gadolinium II samples were cut from the same button of their respective material. None of the holmium samples came from the same button. The gadolinium c-axis I sample is that used by Sill

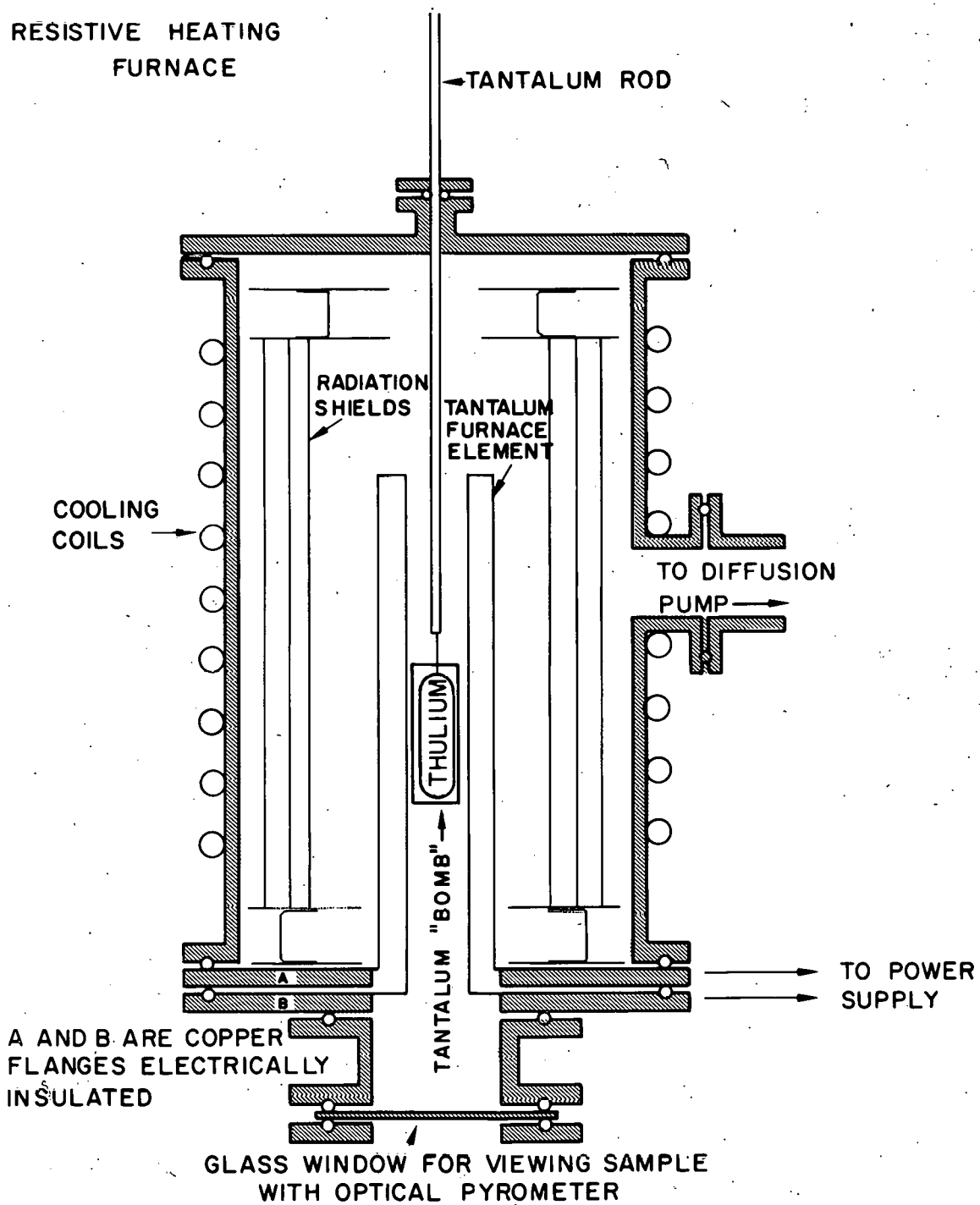
RESISTIVE HEATING FURNACE
TANTALUM ROD
RADIATION SHIELDS
TANTALUM FURNACE ELEMENT
COOLING COILS
TO DIFFUSION PUMP
THULIUM
TANTALUM "BOMB"
A
B
TO POWER SUPPLY
A AND B ARE COPPER FLANGES ELECTRICALLY INSULATED
GLASS WINDOW FOR VIEWING SAMPLE WITH OPTICAL PYROMETER

THIS PAGE

WAS INTENTIONALLY

LEFT BLANK

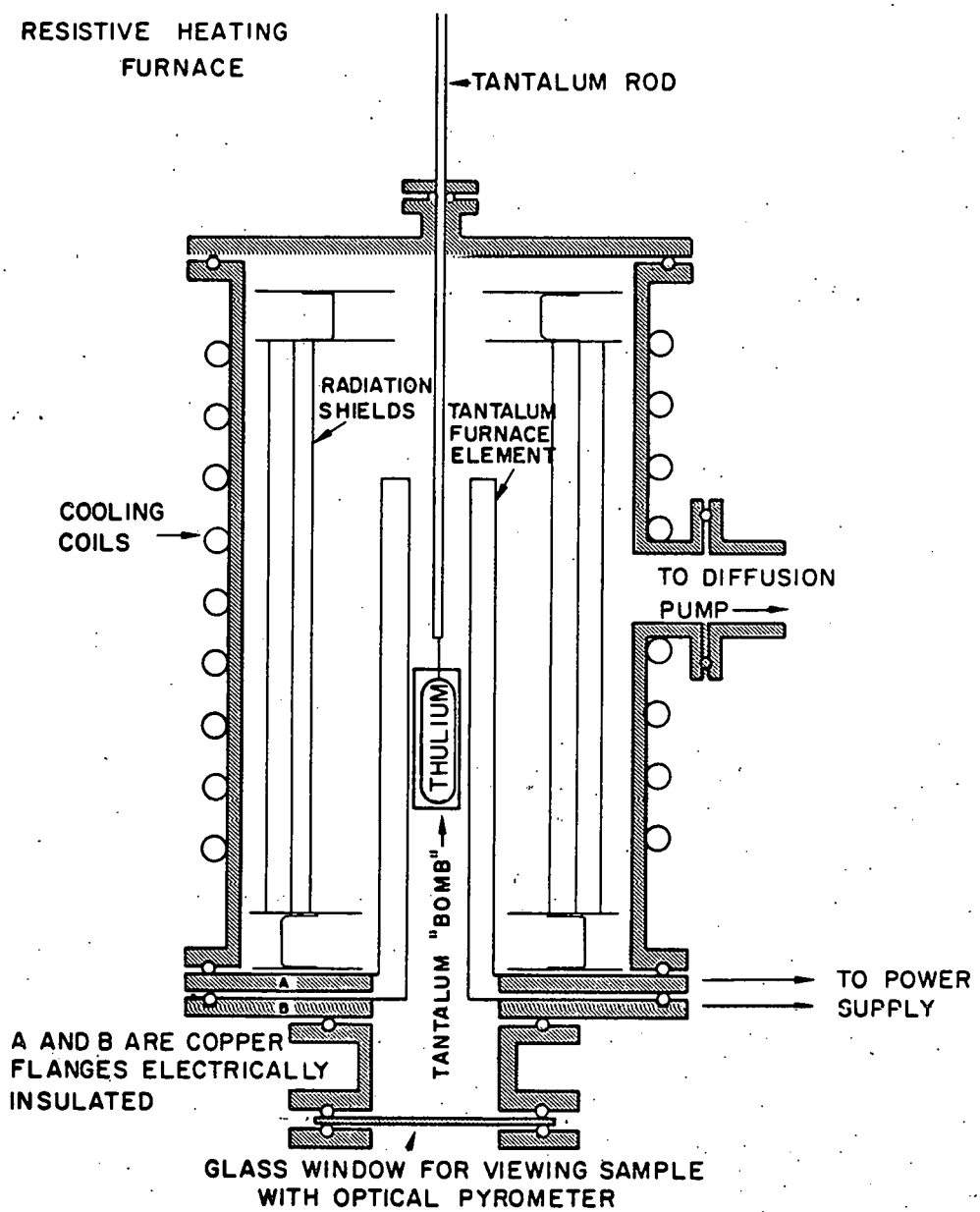

Figure 3. The annealing furnace used for growing single crystals

(53). Scraps of the gadolinium II and terbium buttons left after cutting the samples were spectrographically analyzed for metallic impurities. Gaseous impurities were analyzed by vacuum fusion. The holmium was analyzed prior to annealing. The results are recorded in the Appendix. Final sample dimensions, resistivity ratios, and residual resistivities are also listed in the Appendix.

B. Thermal Conductivity Measurements

Thermal conductivity was measured by the steady state heat flow method. A gradient heater was used to supply a power, $\dot{Q}$, to one end of the sample which would establish a temperature difference, ΔT, across the sample. The length, L, and area, A, of the sample were measured prior to mounting. The thermal conductivity, K, was calculated from the expression

$$\dot{Q} = KA \frac{\Delta T}{L} \quad . \tag{3.1}$$

The dewar and vacuum system is that used by Sill and is described in his thesis (53). The entire system for measuring thermal conductivity was previously used by Boys and is described in his thesis (12). The first measurements were made with his system intact. Certain changes were later made and the following description covers the final state of the apparatus.

The sample holder, shown in Figure 4, is that used by Boys (12). The entire holder was pumped to a vacuum of less than 10^{-5} Torr to minimize heat losses from the gradient heater. Heat leak to the bath was achieved by the No. 24 copper wire. Because of the high vacuum and large number of wires there was sufficient heat leak into the system to preclude achieving the temperature of liquid helium. However, by condensing liquid helium in the 3/8" stainless steel sleeve mounted on the copper heat sink the

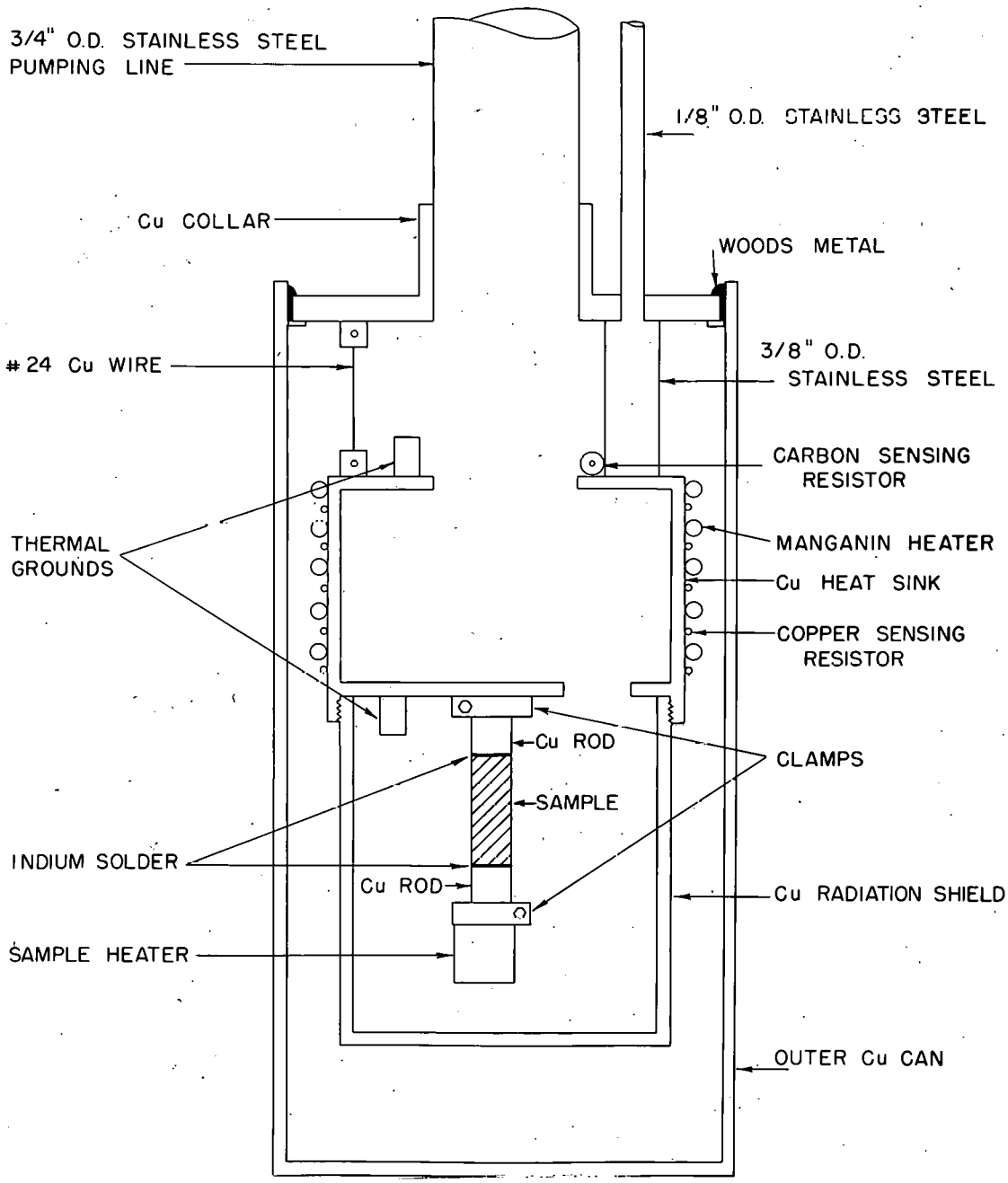
3/4" O.D. STAINLESS STEEL PUMPING LINE
1/8" O.D. STAINLESS STEEL
Cu COLLAR
WOODS METAL
24 Cu WIRE
3/8" O.D. STAINLESS STEEL
CARBON SENSING RESISTOR
THERMAL GROUNDS
MANGANIN HEATER
Cu HEAT SINK
COPPER SENSING RESISTOR
Cu ROD
CLAMPS
SAMPLE
INDIUM SOLDER
Cu ROD
Cu RADIATION SHIELD
SAMPLE HEATER
OUTER Cu CAN

44

THIS PAGE

WAS INTENTIONALLY

LEFT BLANK

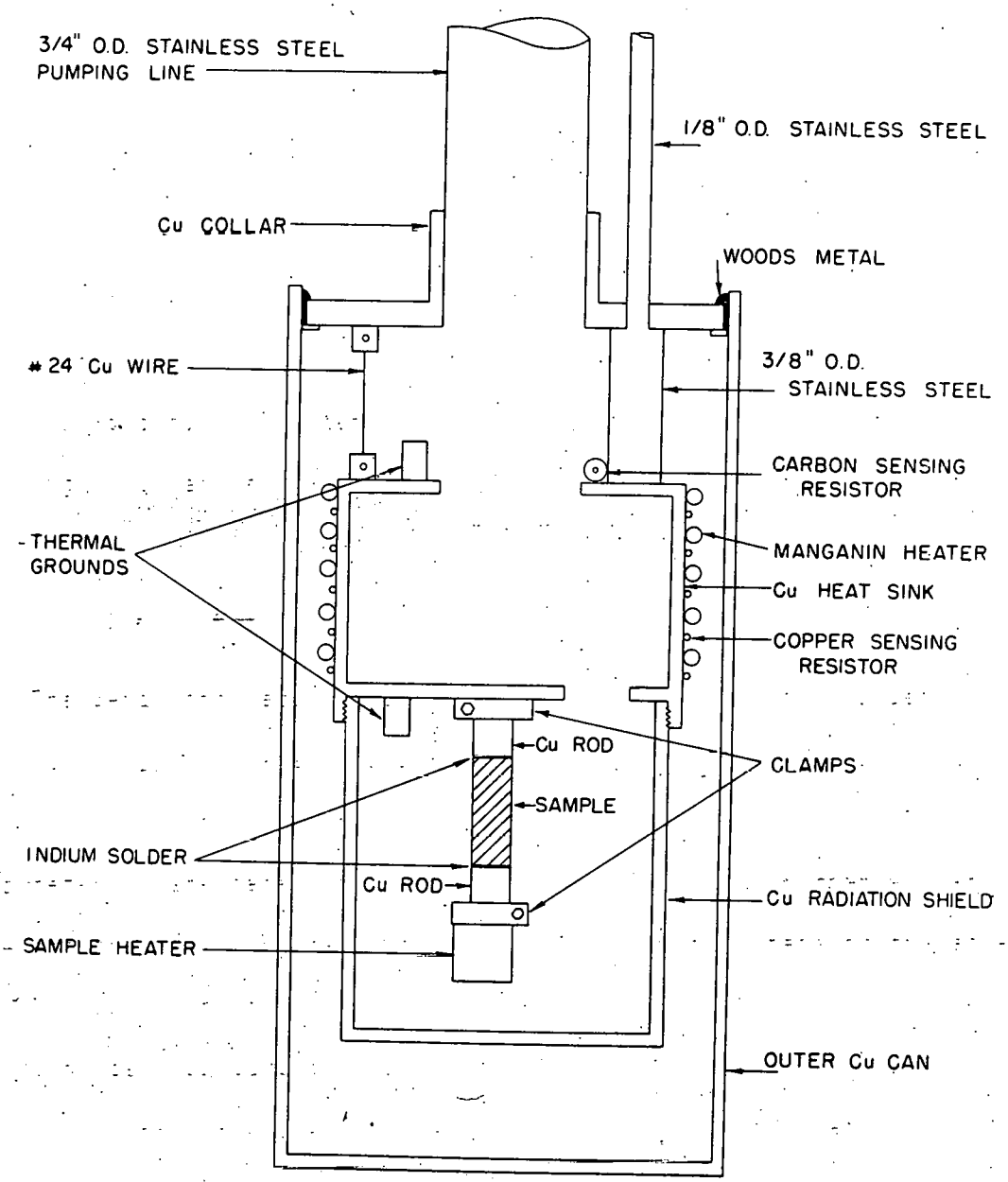

Figure 4. Thermal conductivity sample holder

temperature could be lowered from about $6^{o}K$ to $4.4^{o}K$. The radiation shield keeps the temperature of the surroundings at approximately that of the colder end of the sample and thus minimizes radiation losses. Thermocouples to measure the temperature and temperature difference were mounted in indium at the very tip of the copper rods to which the sample was indium soldered. The temperature control system is described in detail elsewhere (12,54).

This experiment encountered three fundamental problems: solid mounting of the sample, accurate measurement of temperature and temperature difference, and accurate determination of the power flowing through the sample.

Solid mounting of the sample in its holder was essential to insure good thermal contact between the sample and its heaters. If the sample was not mounted properly large thermal contact resistances were introduced and spurious data resulted. Once the sample was inserted properly data was taken on warming from $4.2^{o}K$ to room temperature. Liquid helium was used from 4.2^{o} to $25^{o}K$, liquid hydrogen from 20° to $90^{o}K$, and liquid nitrogen was used from $85^{o}K$ up to room temperature.

The temperature difference across the sample was measured directly. This procedure has two advantages. First, it is more accurate than measuring the temperature at each end and subtracting. Second, by measuring the voltage that corresponds to the temperature difference directly, one can readily observe when the system is coming to equilibrium.

Figure 5 shows the circuit used to measure the temperature and temperature difference. Two thermocouples were inserted at either end of the sample, Cu versus Au-0.03% Fe and Cu versus constantan. The thermocouples anchored to the heat sink were used to measure the absolute temperature.

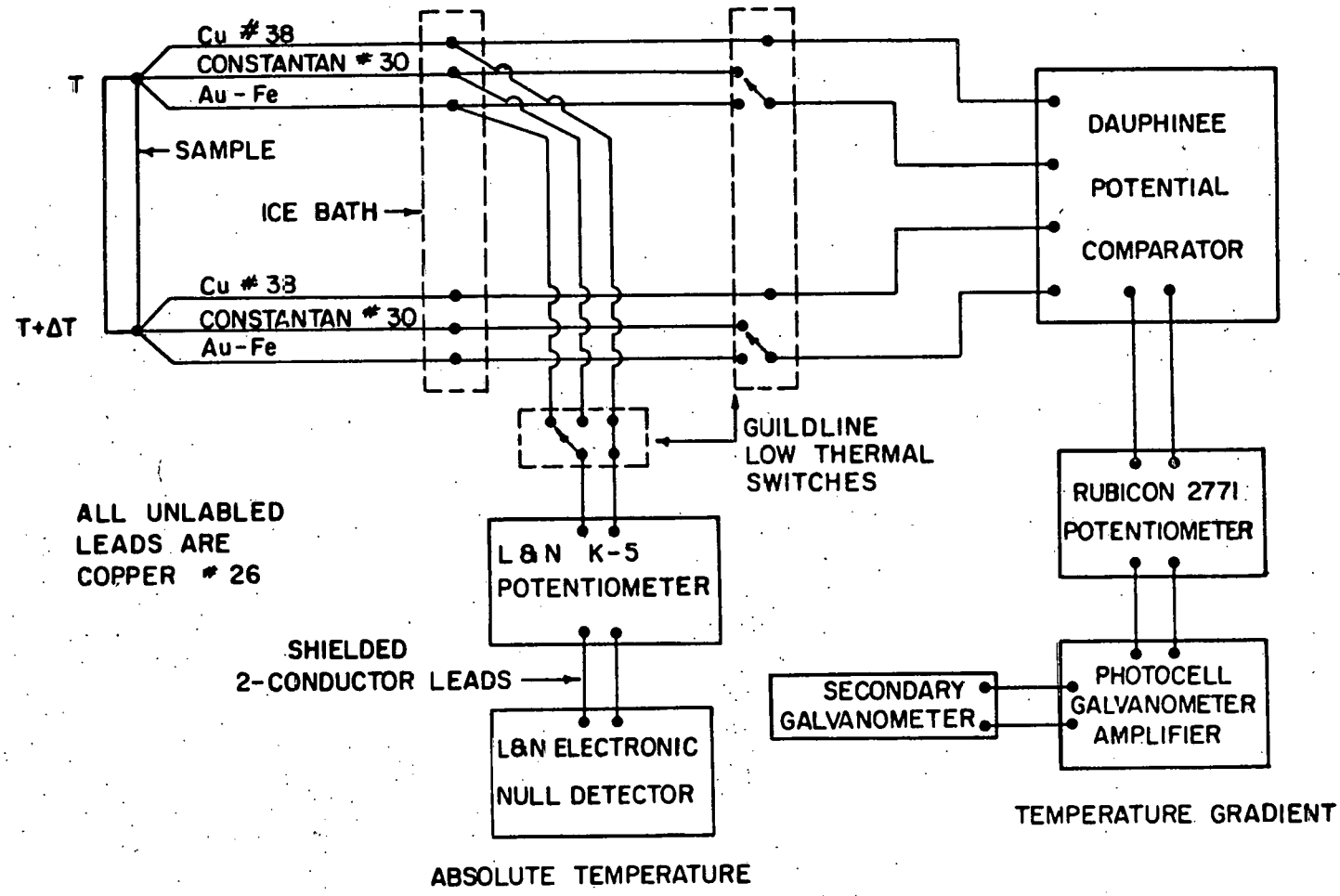

Figure 5. Potentiometric circuit for measuring the temperature and temperature difference

Calibration points were obtained at the bath temperatures of liquid helium, hydrogen, and nitrogen by immersing the thermocouples directly into these liquids. The calibrations were compared to the standard curves for Cu versus constantan obtained by Powell et al. (55) and for Cu versus Au-Fe obtained by Walter Gray of the Ames Laboratory. Due to inhomogeneities in the wire, thermocouples differ at low temperatures. Corrections using the calibration points obtained were made by the method described by Rhyne (54).

Thermocouple voltages corresponding to the absolute temperature were measured with a Leeds and Northrup K-5 potentiometer and a Leeds and Northrup model 9834 null detector. This potentiometer is accurate to 0.3 μV. The relative accuracy of a temperature measurement was 0.1K^{o}, but the absolute accuracy of the calibration procedure is about 0.5K^{o}.

The difference in voltage generated by the thermocouples at either end of the sample is related to the temperature difference. However, because no two thermocouples at the same temperature generate the same emf, a voltage difference can be measured when both thermocouples are in an isothermal environment. This error was calibrated out by measuring the zero temperature difference correction. A copper sample was used to achieve good thermal contact between the two sets of thermocouples. The temperature was varied under experimental conditions from helium to room temperature with the gradient heater off. In this way the correction was measured as a function of temperature.

Thermocouple voltages were subtracted electronically by a Dauphinee potential comparator (56) built by Sill (53). The comparator circuit is shown in Figure 6. The comparator output was measured with a Rubicon model 2771 microvolt potentiometer, Guildline 5214/9660 photocell galvanometer

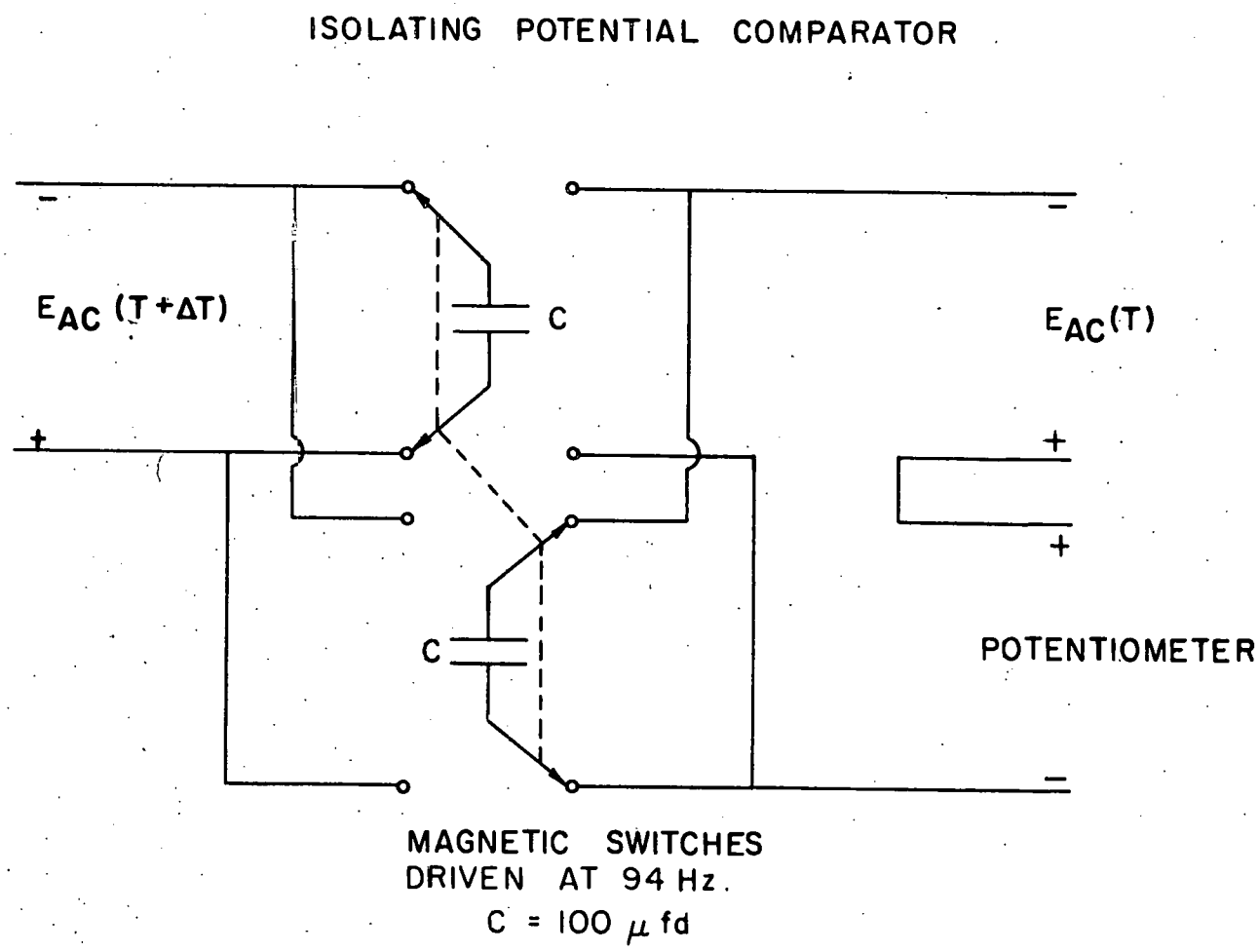

Figure 6. The Dauphinee potential comparator circuit

amplifier, and a Guildline type SR21/9461 secondary galvanometer. This potentiometer can be read to 0.01 μV and has an accuracy of ±0.03 μV.

The temperature difference was calculated by subtracting the zero temperature difference from the comparator output and then dividing by the sensitivity of the thermocouple used. Measured temperature differences ranged from $0.5K^{o}$ at helium temperature up to about $1.5K^{o}$ above nitrogen temperature.

Below $20^{o}K$ the Cu versus Au-Fe thermocouples were used, above $30^{o}K$ the Cu versus constantan, and in the range 20°-$30^{o}K$ both sets of thermocouples were used. Temperature differences often differed by up to $0.1K^{o}$ in this region. To calculate the thermal conductivity the weighted average

$$K = \frac{(30-T)K_{Au-Fe} + (T-20)K_{con}}{10}$$

was used.

Heat leaks by radiation and conduction up lead wires can introduce sizeable errors into a determination of the power flowing through the sample. The problem is compounded by the fact that the rare earths are rather poor thermal conductors.

The power into the gradient heater was measured in two ways. Boys' calibration of heater resistance versus temperature was used in the terbium and gadolinium measurements. The power input was calculated from

$$\dot{Q} = I^2 R_H \quad , \tag{3.2}$$

where I is the current through the heater and R_H is the heater resistance. However, the gradient heater became unstable at the high temperature end of the gadolinium c-axis run and it was necessary to wind a new heater. The second gradient heater was composed of 2200 ohms of one mil manganin wire.

A foot of stronger No. 36 manganin was added to which connections were made. In addition two wires to measure the voltage drop across the heater were inserted into the sample holder. The power could now be calculated from

$$\dot{Q} = IV_H \quad , \tag{3.3}$$

where I is the current through the heater and V_H is the voltage drop across it. This method has the advantage that the power is measured exactly at each data point. However, both methods gave results for the radiation corrections that agreed quite well.

Correction for heat loss through the lead wires attached to the hotter end of the sample and especially for heat loss through radiation was accomplished by the method of Norén and Beckman (57). A sample of essentially zero thermal conductivity is employed. At a fixed temperature a power input, ΔP, into the gradient heater will establish a temperature difference, ΔT, across the "dummy" sample. Since the sample cannot conduct heat (K=0), the heat input is all being radiated to the surroundings or is being conducted up the lead wires from the gradient heater. $\Delta P/\Delta T$ was measured as a function of temperature.

Two radiation correction calibrations were made, each with a different heater and different thermocouples. They agreed with each other and were very close to the results of Boys. The "dummy" samples used were fine thread in one case and a thin piece of wood in the other.

To calculate thermal conductivity at temperature T, $\Delta P/\Delta T$ at T was multiplied by the measured temperature difference. The correction was then subtracted from the measured power input. This procedure was followed above 80°K.

The circuit to measure the power input is shown in Figure 7. A rubicon Type B potentiometer and Leeds and Northrup model 2430 galvanometer were used to measure the gradient heater current by measuring the voltage across a one ohm standard resistor. This potentiometer is accurate to $\pm 1\ \mu V$. The voltage across the heater was measured with a Keithley model 622 differential voltmeter, accurate to $\pm 0.1\%$.

C. Electrical Resistivity Measurements

The electrical resistivity measurements were made by the standard four-probe technique described by Colvin *et al*. (58). All measurements were made in the apparatus built by Edwards and described in his thesis (15).

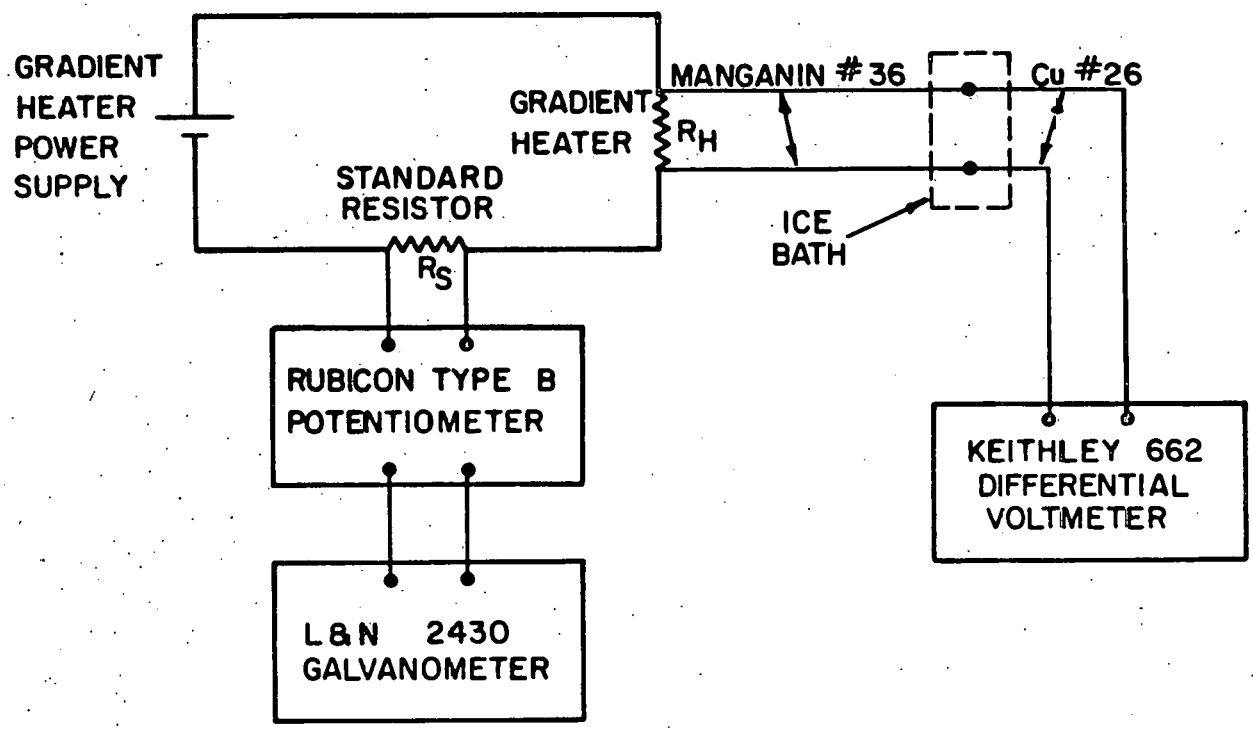

Figure 7. The circuit for measuring the power input to the gradient heater

IV. RESULTS

A. Thermal Conductivity

Transport properties of rare earth metals exhibit anomalous behavior near known magnetic transition temperatures. Before describing the results of this study it is, therefore, appropriate to describe the magnetic structure of gadolinium, terbium, and holmium.

Cable and Wollan (59) by means of neutron diffraction have shown that gadolinium orders only in the ferromagnetic state. Between $T_c = 294^oK$ and $T = 232^oK$ the moment is along the c-axis. Below 232^oK it moves away from the c-axis to a maximum deviation of about 65° at 180^oK and then back to within 32° of the c-axis at low temperatures. Nigh et al. (9) by means of magnetic moment measurements on single crystals showed gadolinium to have a Curie point of 293^oK.

Koehler et al. have observed the magnetic structure of terbium (60) and holmium (61) by neutron diffraction. Their findings are illustrated in Figure 8. The transition temperatures indicated were obtained by Hegland et al. (10) for terbium and Strandburg et al. (13) for holmium by magnetic moment measurements. Terbium is ferromagnetic up to 221^oK, helical antiferromagnetic to 230^oK, and paramagnetic at higher temperatures. Holmium is conical ferromagnetic up to 20^oK, helical antiferromagnetic to 132^oK, and paramagnetic at higher temperatures.

The thermal conductivity of gadolinium is shown in Figure 9. This data was taken on the gadolinium II samples. The curves for both axes exhibit characteristic low temperature peaks. The c-axis conductibility, K_c, drops off faster than the a-axis (basal plane) conductivity, K_a. K_c is

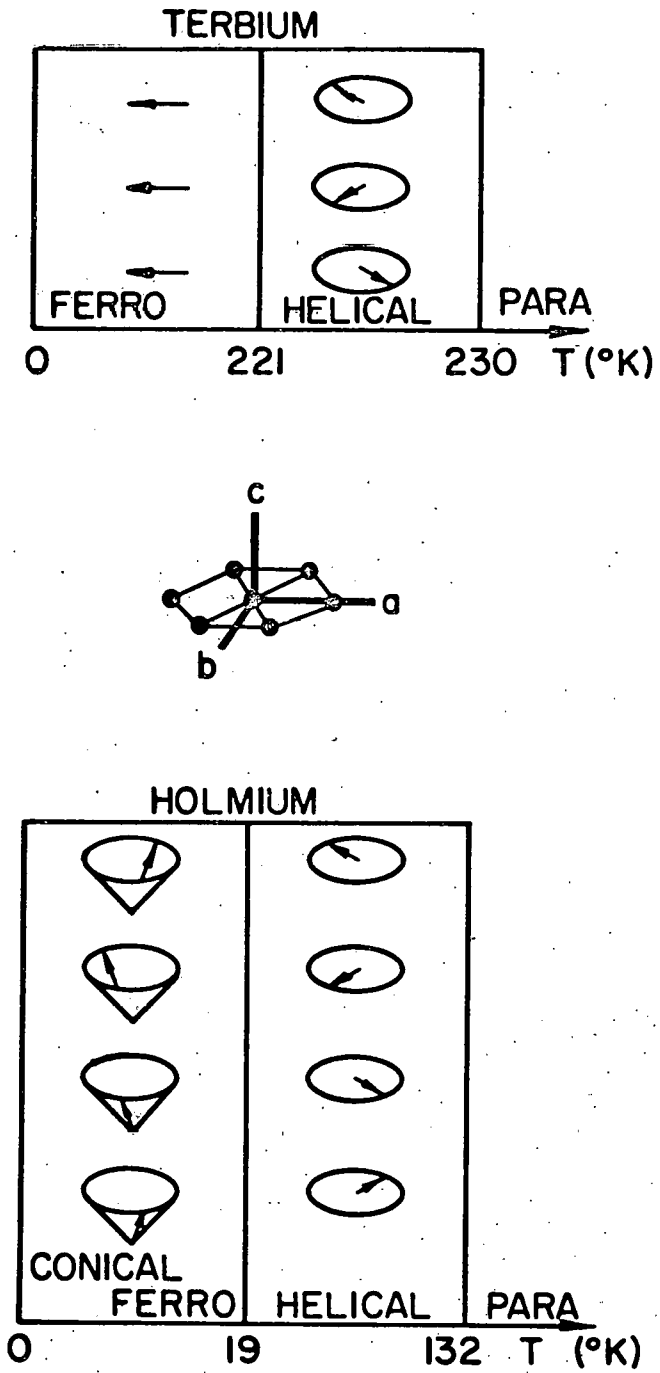

Figure 8. The ordered spin structure of terbium and holmium as observed by neutron diffraction

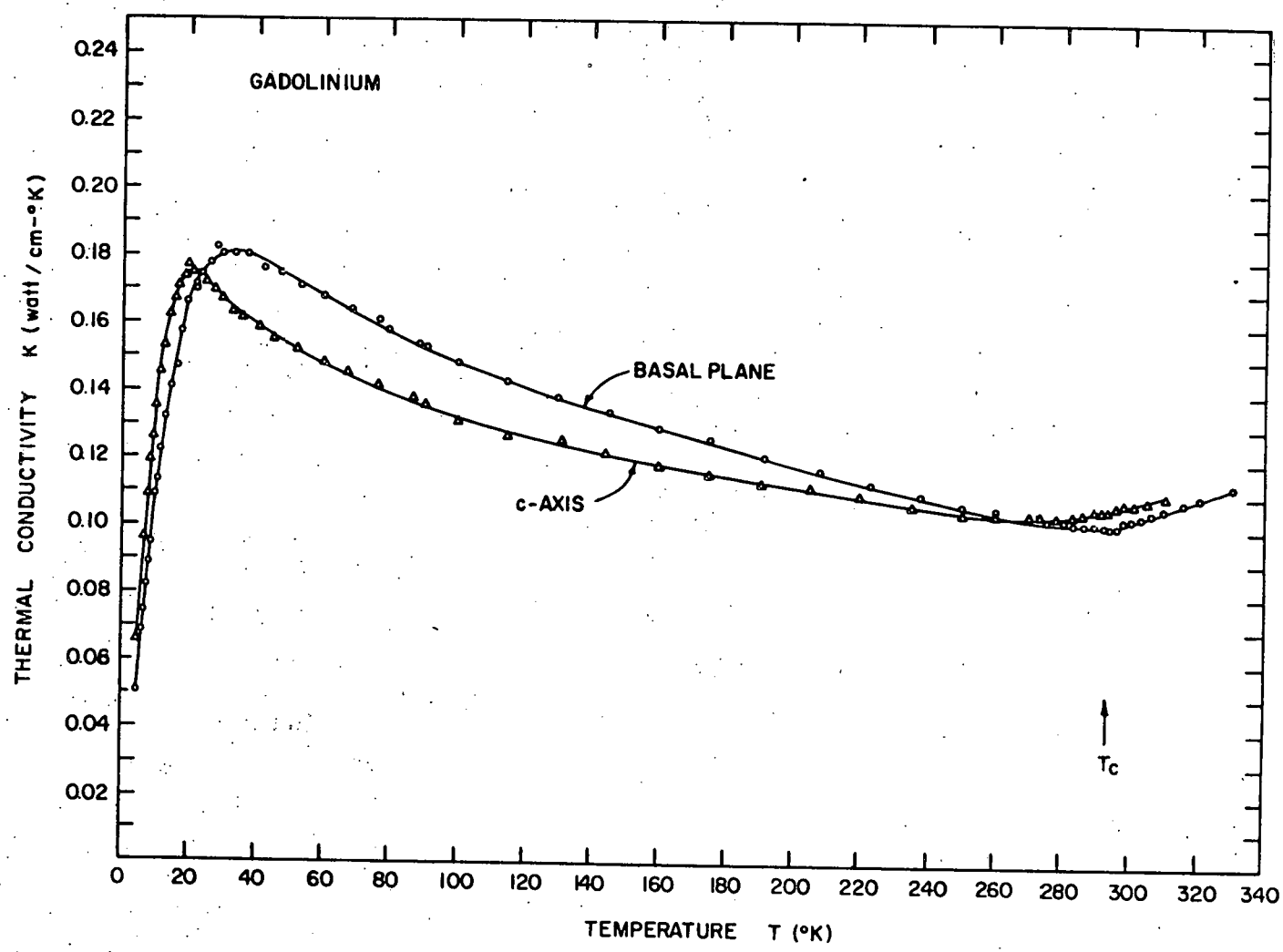

Figure 9. Thermal conductivity of single-crystal gadolinium as a function of temperature

less than K_a from 22° to 265^oK. The a-axis conductivity undergoes an abrupt change in slope at 294^oK and rises linearly up to 330^oK. K_c goes through a minimum at 275^oK and passes smothly through the Curie point at 293^oK.

The thermal conductivity of terbium is shown in Figure 10. Terbium is very anisotropic ($K_c/K_a \simeq 1.5$ over the whole temperature range). Both axes have low temperature peaks near 25^oK and drop off equally fast at higher temperatures. The c-axis conductivity evidences both the ferromagnetic-antiferromagnetic transition and the magnetic order-disorder transition. K_c is fairly flat from 222^oK to 230^oK and increases above the Néel point. K_a shows little indication of the Curie point but does experience a change of slope at 231^oK. K_a also increases above the Néel point. Figure 11 shows the thermal conductivity of terbium on an enlarged scale in the region of the magnetic transitions.

The thermal conductivity of holmium is shown in Figure 12. Holmium also is very anisotropic over the whole temperature range. The c-axis conductivity has a 1% drop at 20^oK, the Curie point, while K_a has a peak at the same temperature. Both axes increase until about 55^oK. K_c drops off to a minimum at 110^oK, rises until 132^oK, the Néel point, undergoes a slope change at this temperature, and then increases steadily up to room temperature. K_a passes through a minimum at the Néel point, and rises steadily to its room temperature value.

Impurities have a pronounced affect on the thermal conductivity. Figure 13 shows the thermal conductivity of two gadolinium samples. The gadolinium c-axis II data is the same as that of Figure 9. The gadolinium I sample was very long and narrow; i.e., L/A was large. Hence, little

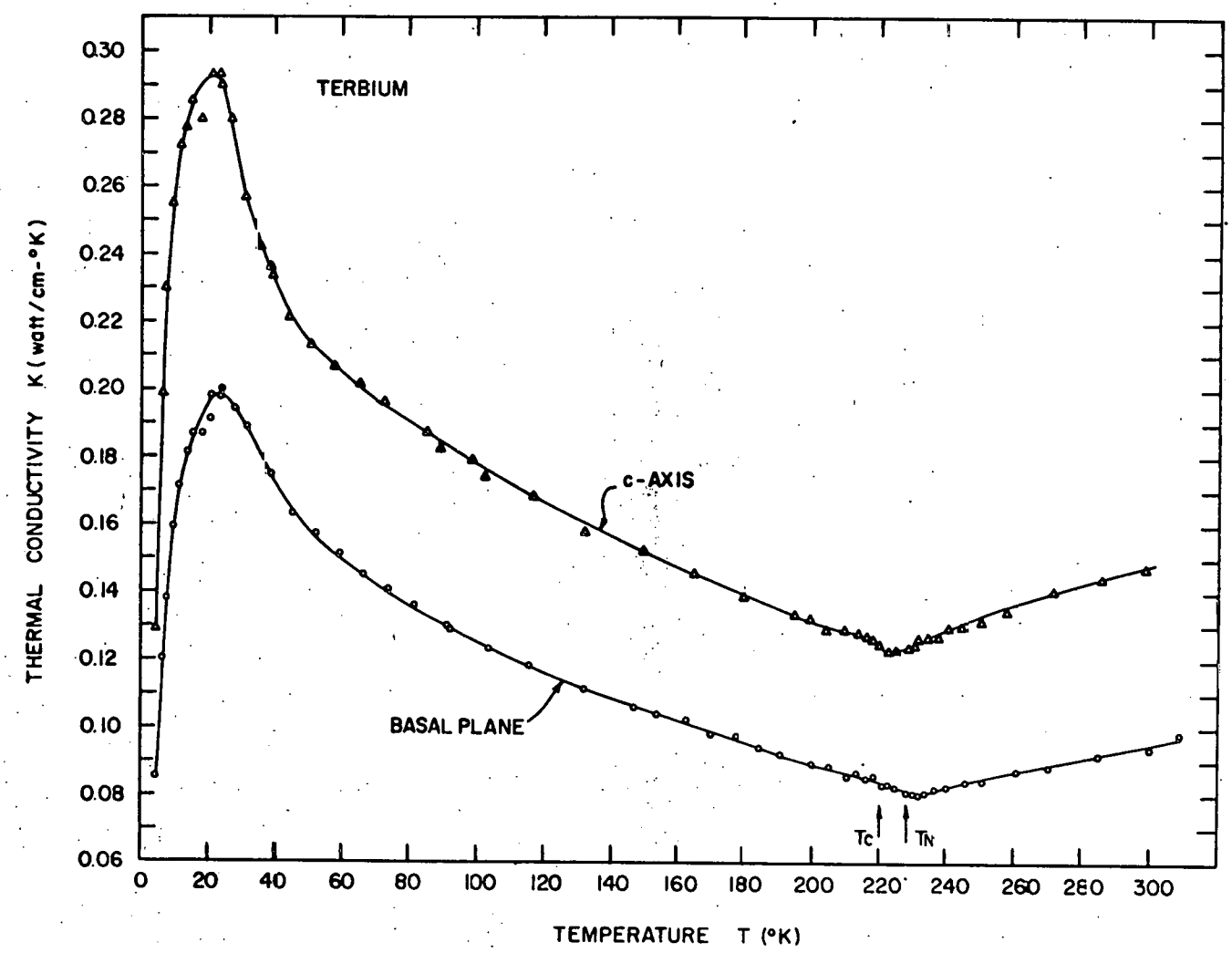

Figure 10. Thermal conductivity of single-crystal terbium as a function of temperature

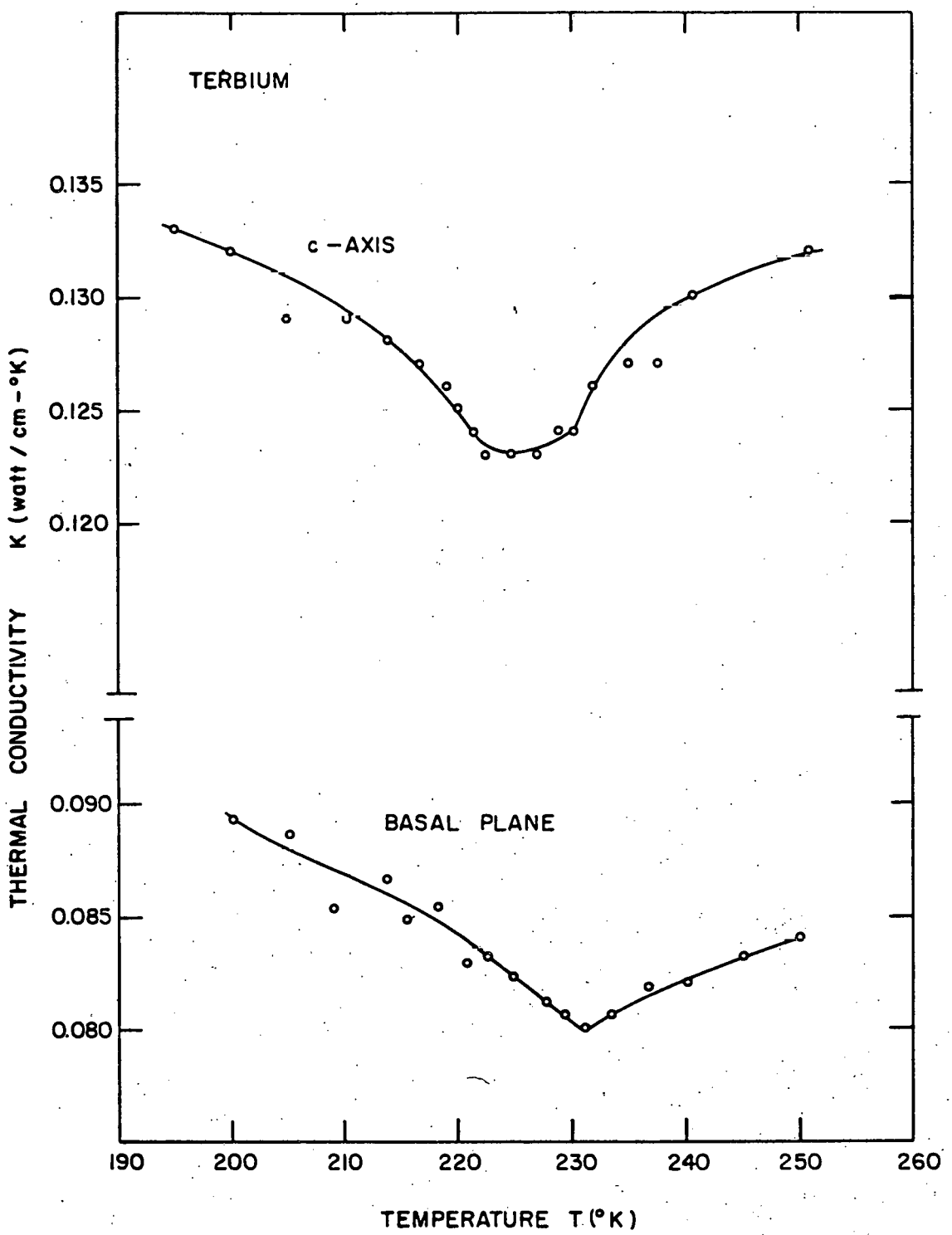

Figure 11. Thermal conductivity of terbium in the region of the magnetic transitions

THIS PAGE

WAS INTENTIONALLY

LEFT BLANK

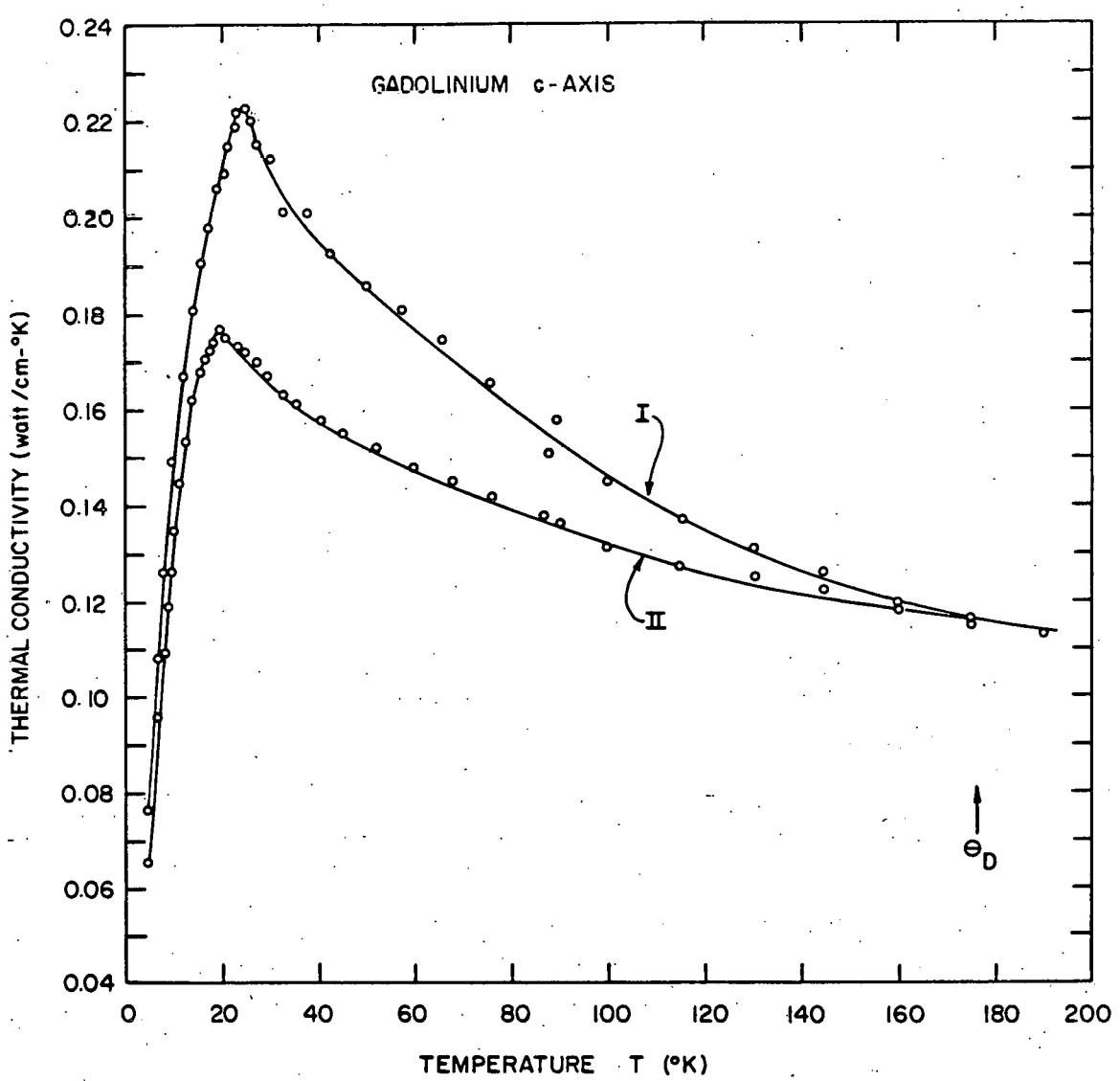

Figure 13. Thermal conductivity of two gadolinium c-axis samples

power was needed to establish a temperature gradient across this sample and near 200°K the measured power input was very close to the radiation correction. Reliable data could not be taken above about 180°K for this sample. Curves for the two samples have generally the same shape. The difference at low temperatures can be attributed to impurities. As the Debye temperature is approached impurity effects should be less important and the thermal conductivities of different samples of the same material tend to the same value. The thermal conductivities of these two samples do approach the same value near the Debye temperature, θ_D. Also, both c-axis thermal conductivities eventually dip below that of a-axis II in the ferromagnetic region.

Figure 14 is another example of the influence of impurities. The holmium a-axis II is the same as that of Figure 12. The holmium a-axis I has a residual resistivity of 15.2 μΩ-cm; the holmium a-axis II sample has a residual resistivity of 2.8 μΩ-cm. The curves here do not have the same shape at low temperatures. Equation 2.11 says that the thermal conductivity should be proportional to T in the residual resistance region. The residual resistivity is never less than 80% of the total resistivity up to 20°K for sample I. The residual resistivity dominates in this region and the thermal conductivity is linear up to 20°K. Sample II, however, is much more pure and gives a better indication of the ideal thermal conductivity of holmium. The Néel point of sample I also appears to be shifted a few degrees lower than that of sample II. There is no tendency for the curves to approach the same value near θ_D because spin disorder scattering is prominent in this region for holmium. More will be said about this point later.

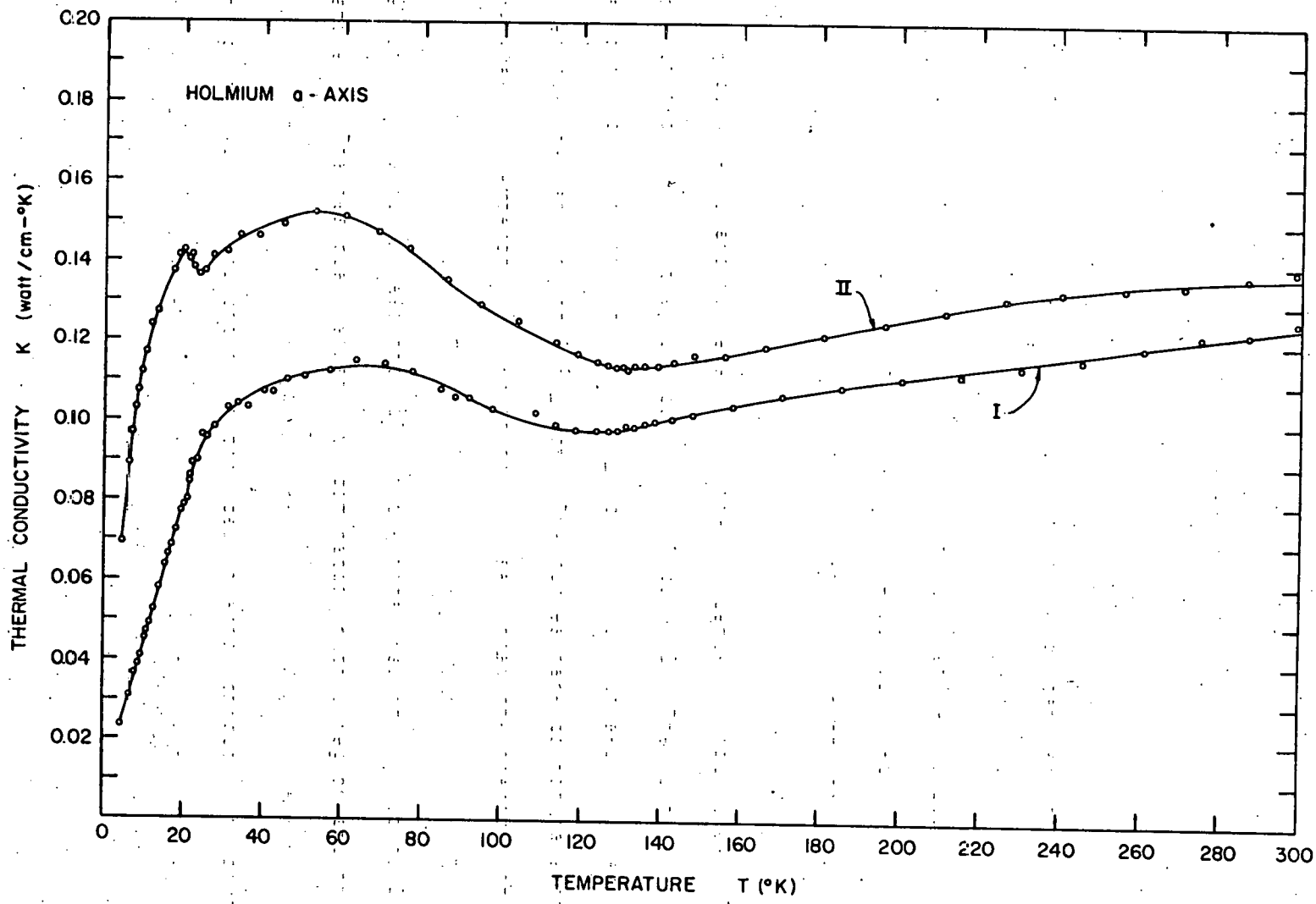

Figure 14. Thermal conductivity of two holmium a-axis samples

B. Electrical Resistivity

The electrical resistivities of the samples were measured to determine accurately the Lorenz functions. The gadolinium results agreed very well with the results of Nigh et al. (9), and are not shown in a Figure. Variation between the two sets of data ranged between 0-3%. The electrical resistivities of the terbium and holmium samples varied by 6-7% with previous data near room temperature.

The electrical resistivity of terbium is shown in Figure 15. The resistivity is relatively isotropic in the ferromagnetic region, while above the Néel point the resistivity is markedly anisotropic. The a-axis resistivity, ρ_a, shows slope changes at about 219°K and at 230°K. The c-axis resistivity, ρ_c, shows a sudden 3% increase between 219°-220°K and a change of slope at 229°K. The electrical resistivity of terbium in the region of the magnetic transitions is shown in Figure 16.

The electrical resistivity of holmium is shown in Figure 17. Both ρ_a and ρ_c exhibit slight changes of slope at 20°K. Below 100°K the resistivity is essentially isotropic. Above 100°K, ρ_a continues to increase up to the Néel temperature, shows a slope change at 130°K, and rises linearly at higher temperatures. The c-axis resistivity exhibits a broad peak, which is characteristic of antiferromagnets below the Néel point, shows a large change of slope at 131°K, and increases linearly above 200°K.

C. Lorenz Function

The Lorenz functions of gadolinium, terbium, and holmium are shown in Figures 18, 19, and 20. The Lorenz functions of all these samples have several characteristics in common. These functions have minima at low

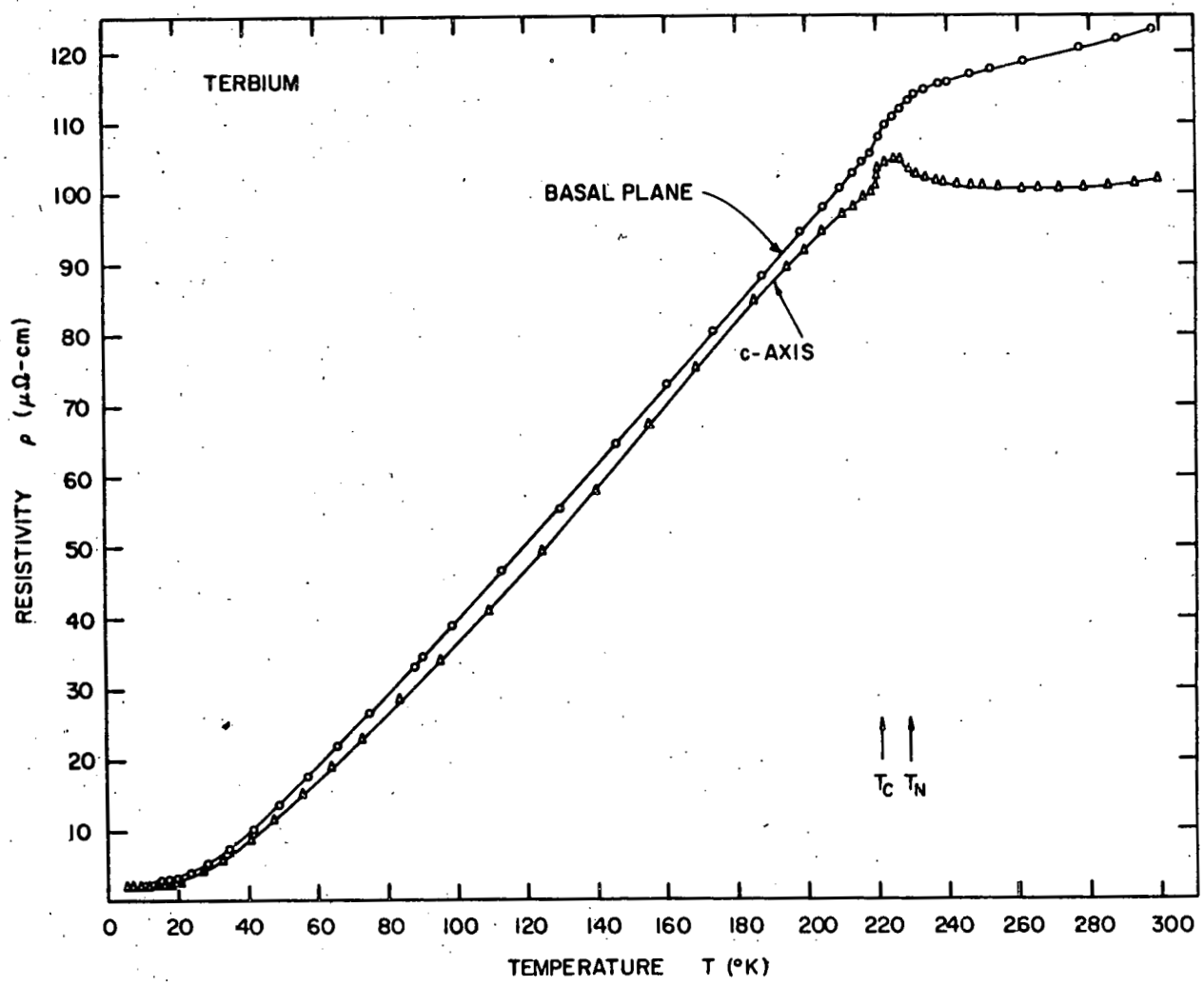

Figure 15. Electrical resistivity of single-crystal terbium as a function of temperature

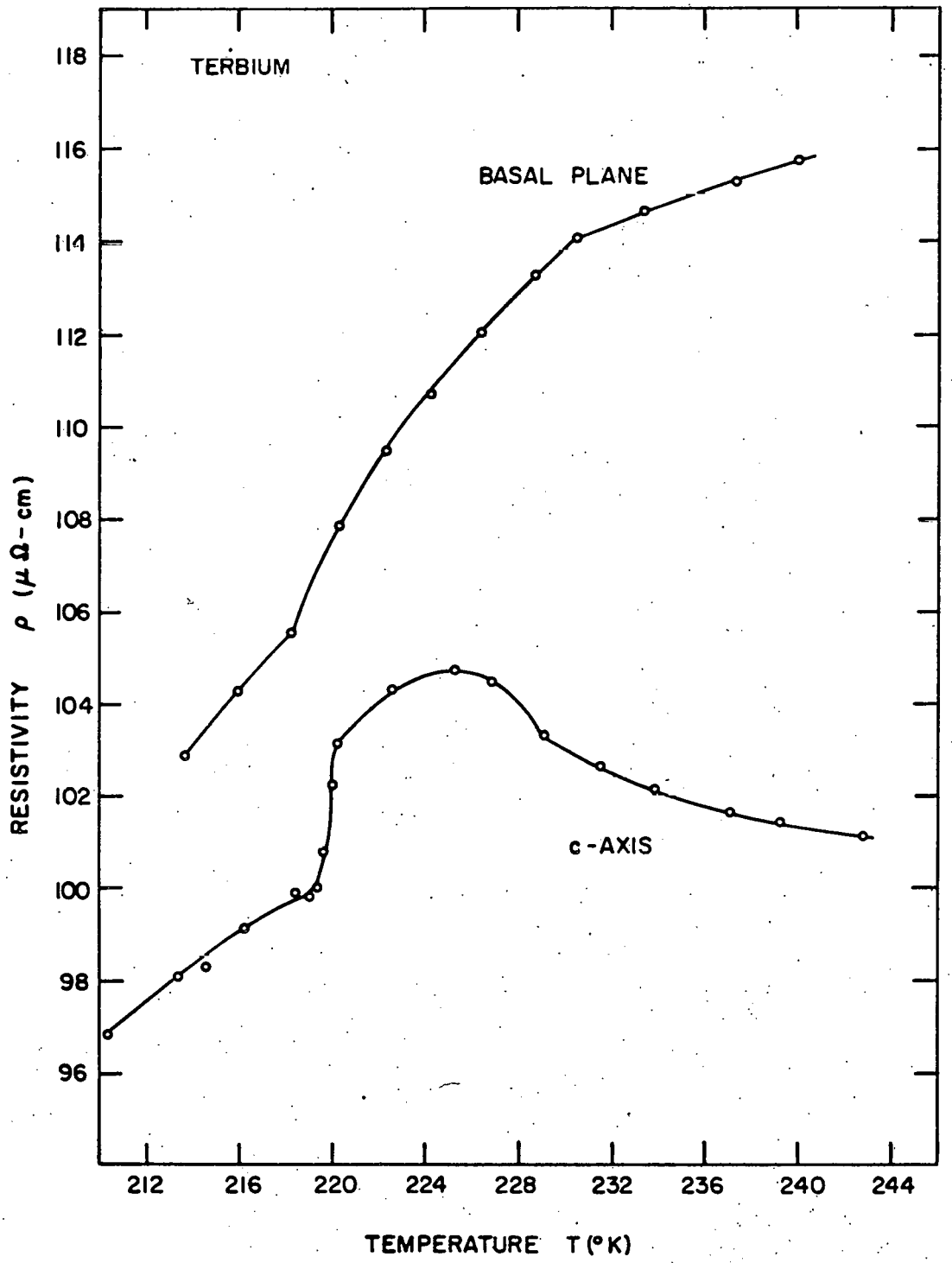

Figure 16. Electrical resistivity of terbium in the region of the magnetic transitions

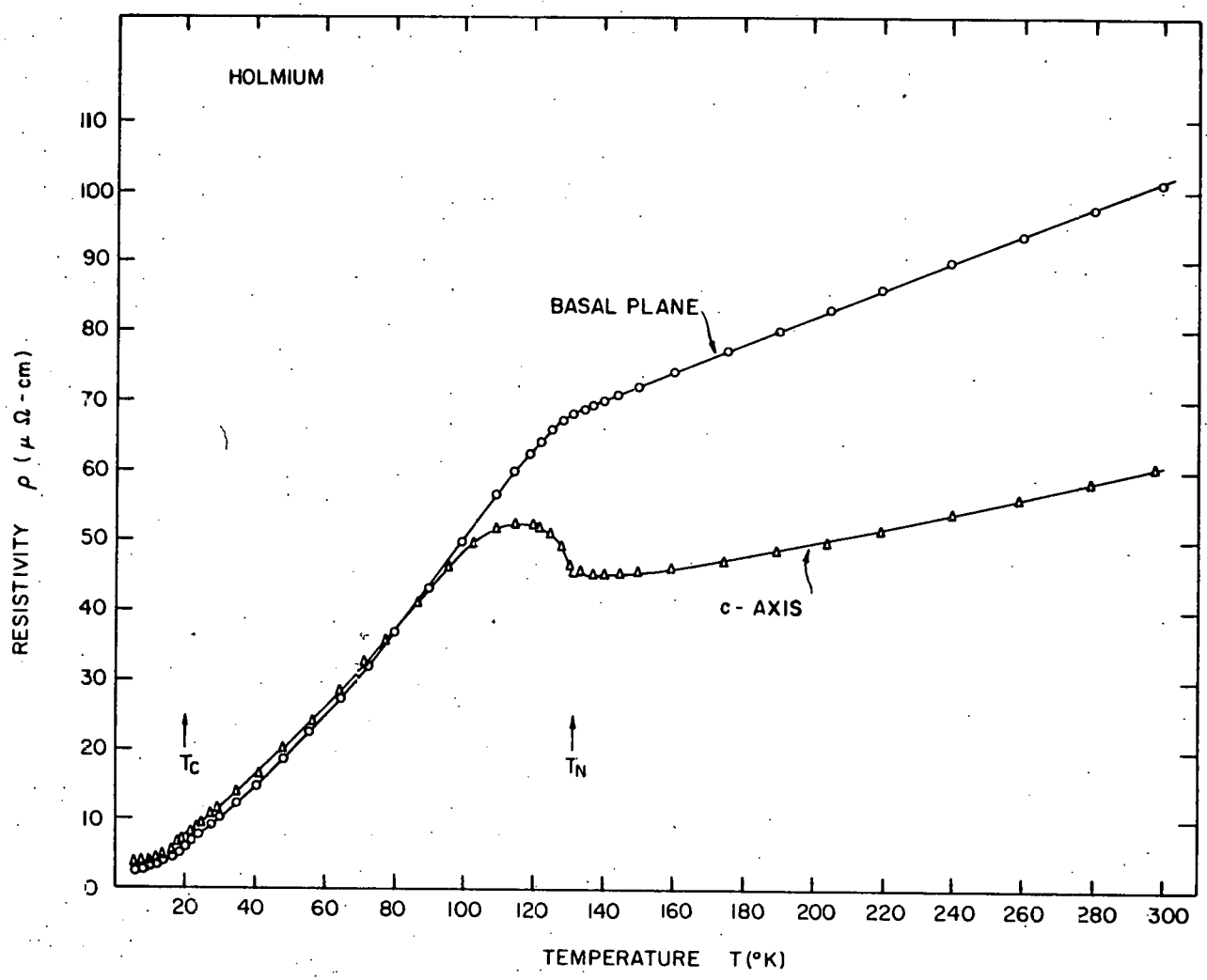

Figure 17. Electrical resistivity of single-crystal holmium as a function of temperature

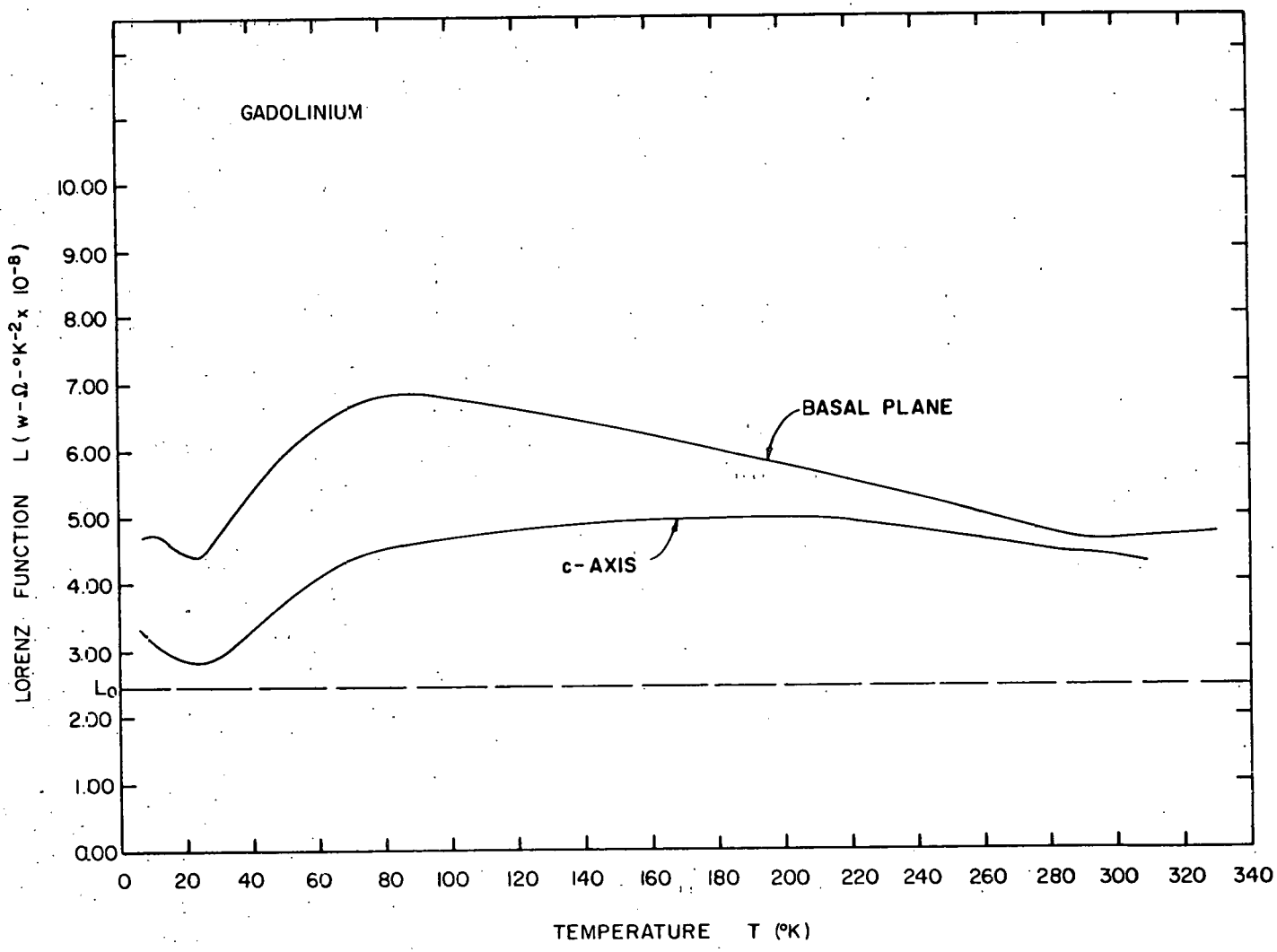

Figure 18. Lorenz function of single-crystal gadolinium

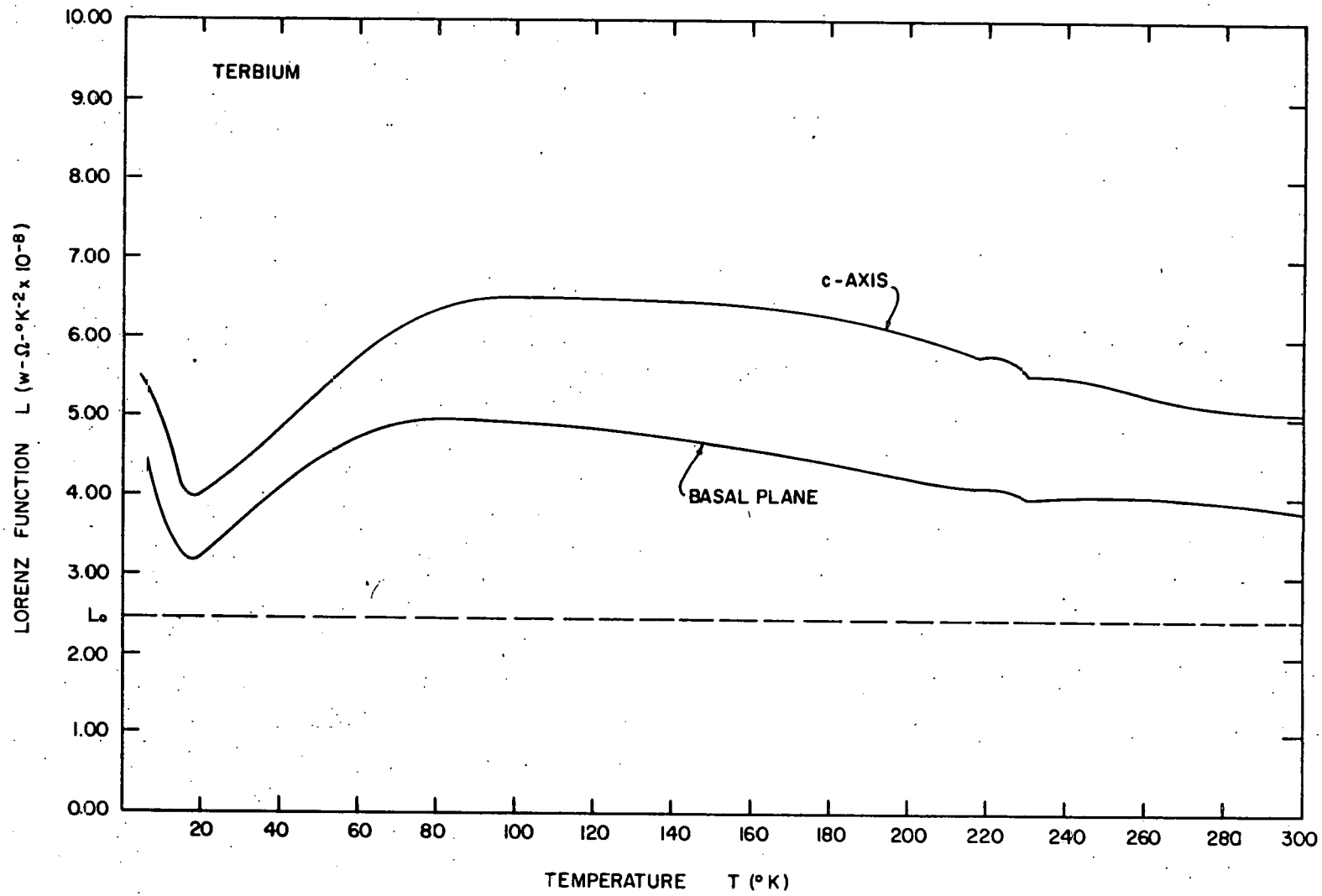

Figure 19. Lorenz function of single-crystal terbium

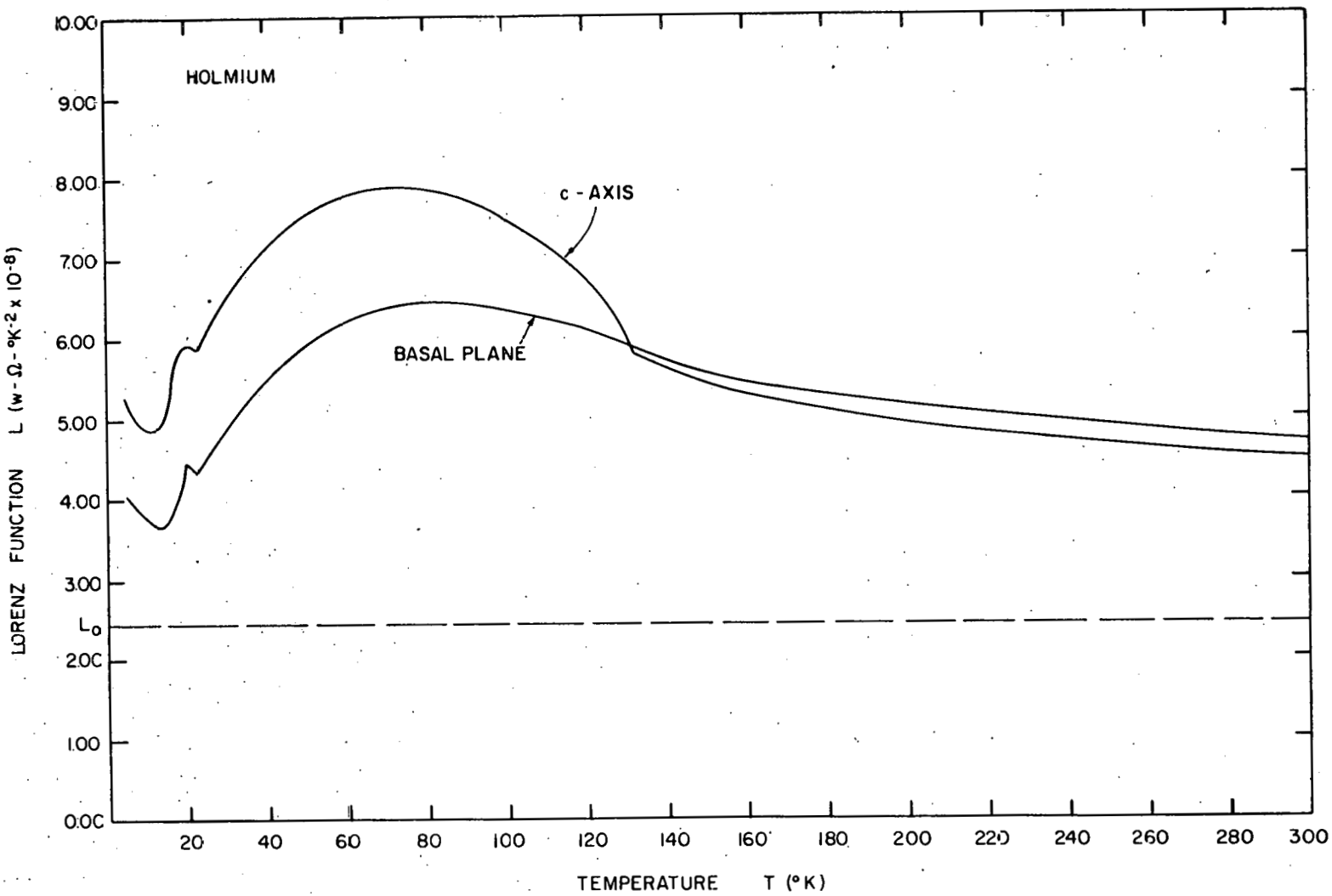

Figure 20. Lorenz function of single-crystal holmium

temperatures, the largest values are at intermediate temperatures, and the Lorenz functions are rather slowly varying in the paramagnetic regions. At low temperatures impure samples have higher Lorenz numbers than more pure samples. At $5^{o}K$ the holmium a-axis I and the holmium a-axis II samples have Lorenz numbers of 7.65×10^{-8} and 3.96×10^{-8} watt-ohm/$^{o}K^{2}$, respectively. The resistivities of these two samples at this temperature are 15.2 and 2.8 $\mu\Omega$-cm, respectively. This phenomenon has been observed previously. For example, White and Woods (62) found similar results in their comprehensive study of the electrical and thermal resistivity of polycrystalline transition elements.

V. DISCUSSION

The electrical resistivity and thermal conductivity are, in general, second rank tensors. For metals with hexagonal symmetry the principal axes are the a-axis ([$11\bar{2}0$] direction), the b-axis ([$10\bar{1}0$] direction), and the c-axis ([0001] direction). In addition, Boas and Mackenzie (63) have shown that for a hexagonal lattice there will be no basal plane anisotropy in properties which can be represented by a linear relation between two vectors. Both the electrical resistivity and thermal conductivity are defined by such relations. Hence, both of these tensor quantities are completely determined when the charge current and the heat current flow along the c-axis and along either the a-axis or b-axis. In this investigation all measurements were made along the a-axis and along the c-axis.

Any discussion of the transport properties of the rare earth metals must begin with a discussion of the electronic structure of these metals. Figure 21 shows the band structure of gadolinium along the symmetry direction Γ-K-H-A as calculated by Freeman *et al*. (64). Keeton and Loucks (4) have recently made relativistic calculations of the band structure and Fermi surface of gadolinium. Their results are essentially the same as those of Freeman *et al*. except that the degeneracy in the plane A-L-H is removed.

Below the Curie point the conduction band is split due to an exchange interaction between the conduction electrons and the 4f electrons. On the basis of their calculated density of states at the Fermi level and a saturation magnetization of 7.55 Bohr magnetons per atom, Freeman *et al*. (64) estimate the band splitting in gadolinium at $T=0^{o}K$ to be 0.61 ev. The

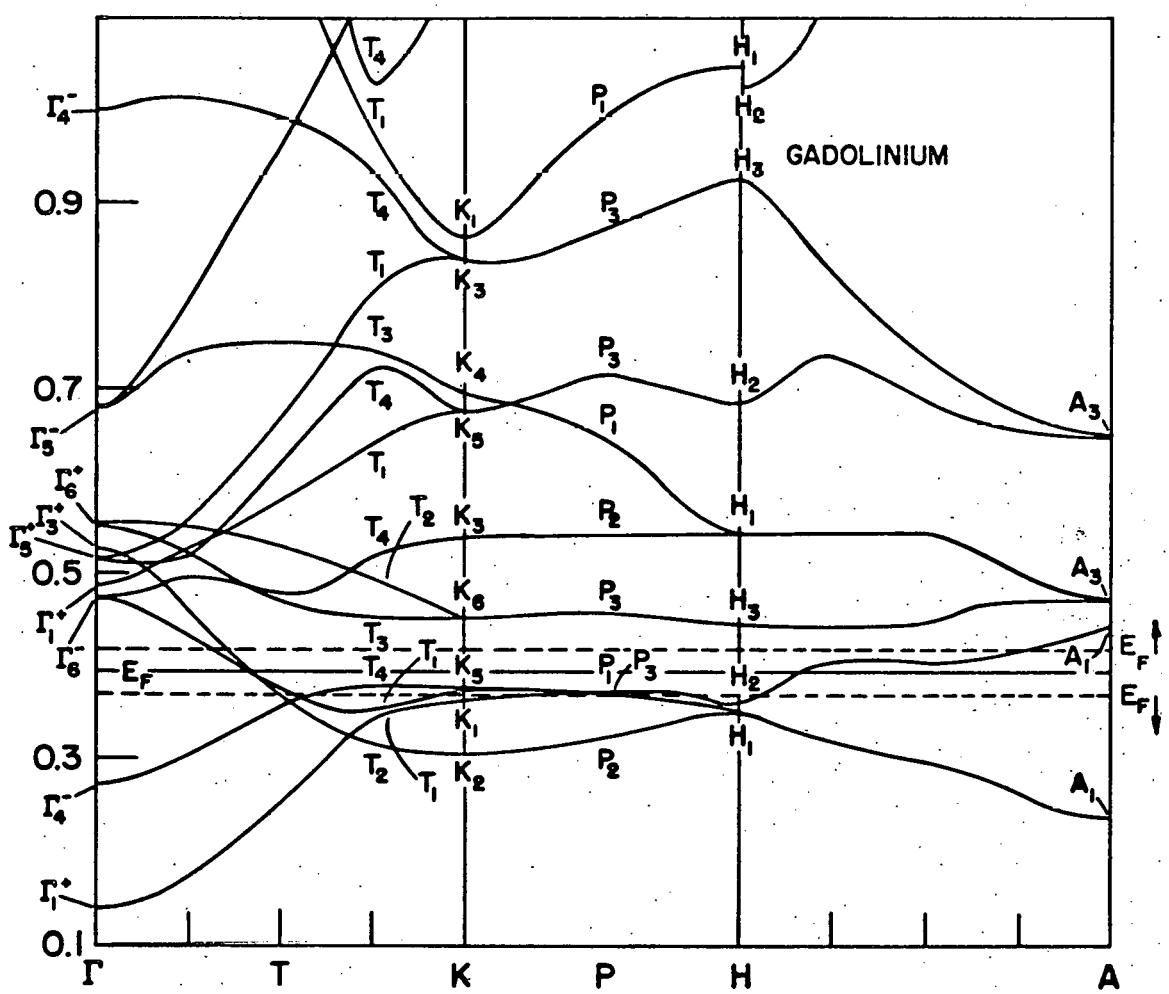

Figure 21. Band structure of gadolinium along the symmetry direction Γ-K-H-A as calculated by Freeman et al. (64)

Fermi levels of the spin up and spin down electrons have been indicated in Figure 21.

Figure 22 shows the Fermi surface of gadolinium as calculated by Freeman et al. (64). It is very anisotropic. Figure 23a is an attempt to determine how the Fermi surface of gadolinium is distorted at low temperatures by band splitting. This diagram was drawn with the assistance of S. H. Liu. It is completely qualitative. Intersections of the various Fermi levels of Figure 21 with the conduction bands were marked on the perimeter of the rectangle Γ-K-H-A. The shapes of the curves joining the various intersections on the perimeter were estimated. It is expected that the ferromagnetic Fermi surface may be distorted with temperature, since it is not unlikely that the band splitting may have the same temperature dependence as the spontaneous magnetization. Also implicit here is the assumption that the energy bands are not themselves altered below the Curie temperature. Thus, let it be emphasized that the figure was drawn qualitatively to qualitatively explain the isotropic resistivity of gadolinium and terbium in the ferromagnetic state.

Terbium should have a band structure similar to that of gadolinium. This statement is made plausible by comparing the electrical resistivity of gadolinium with the resistivity of terbium. In the ferromagnetic region of both metals the shape and magnitude of the resistivity curves are quite similar. The resistivity of both metals is essentially isotropic below the Curie point and anisotropic above the magnetic ordering temperature.

The electrical conductivity can be expressed as

$$\sigma_{ii} = \frac{e^2\tau}{4\pi^3\hbar} \int_{E_F} v_i dS_i \quad . \tag{2.9a}$$

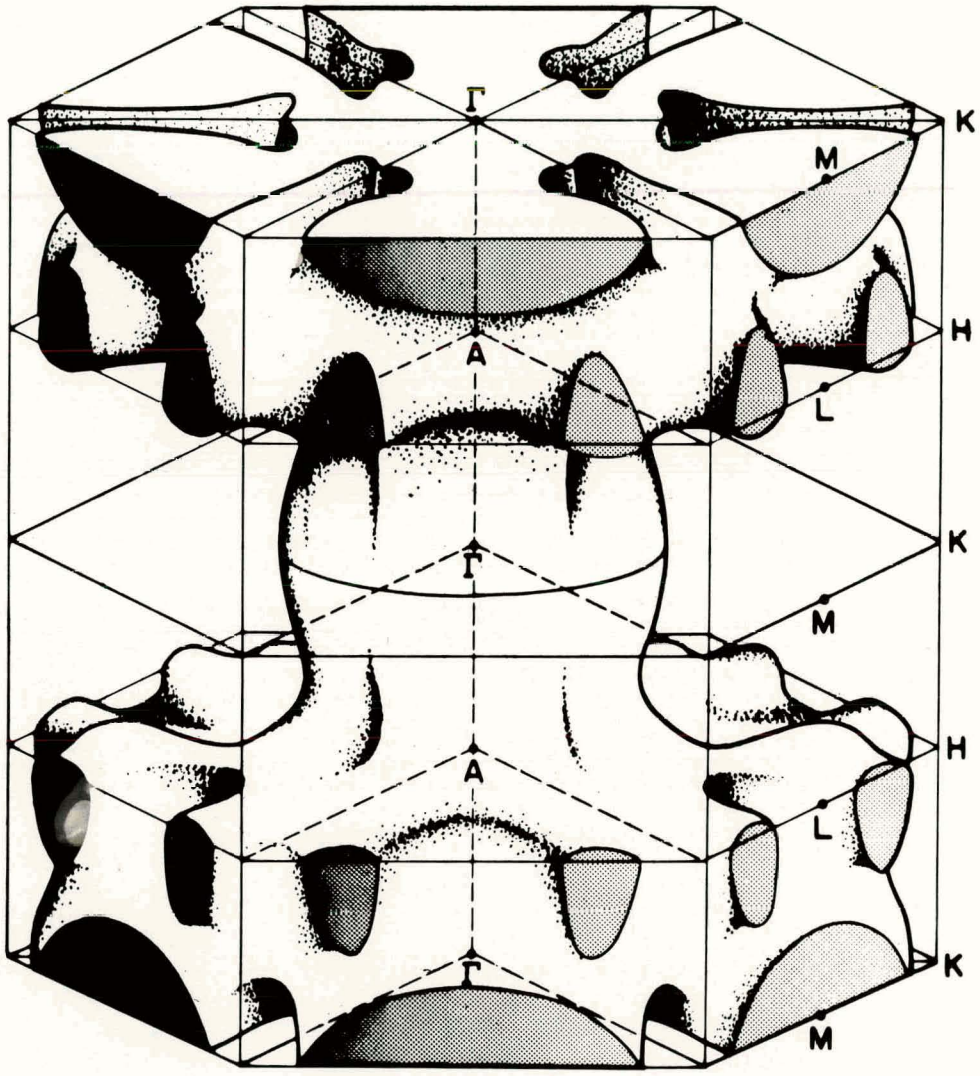
Γ
K
M
H
A
L
K
Γ
M
H
A
L
K
Γ
M

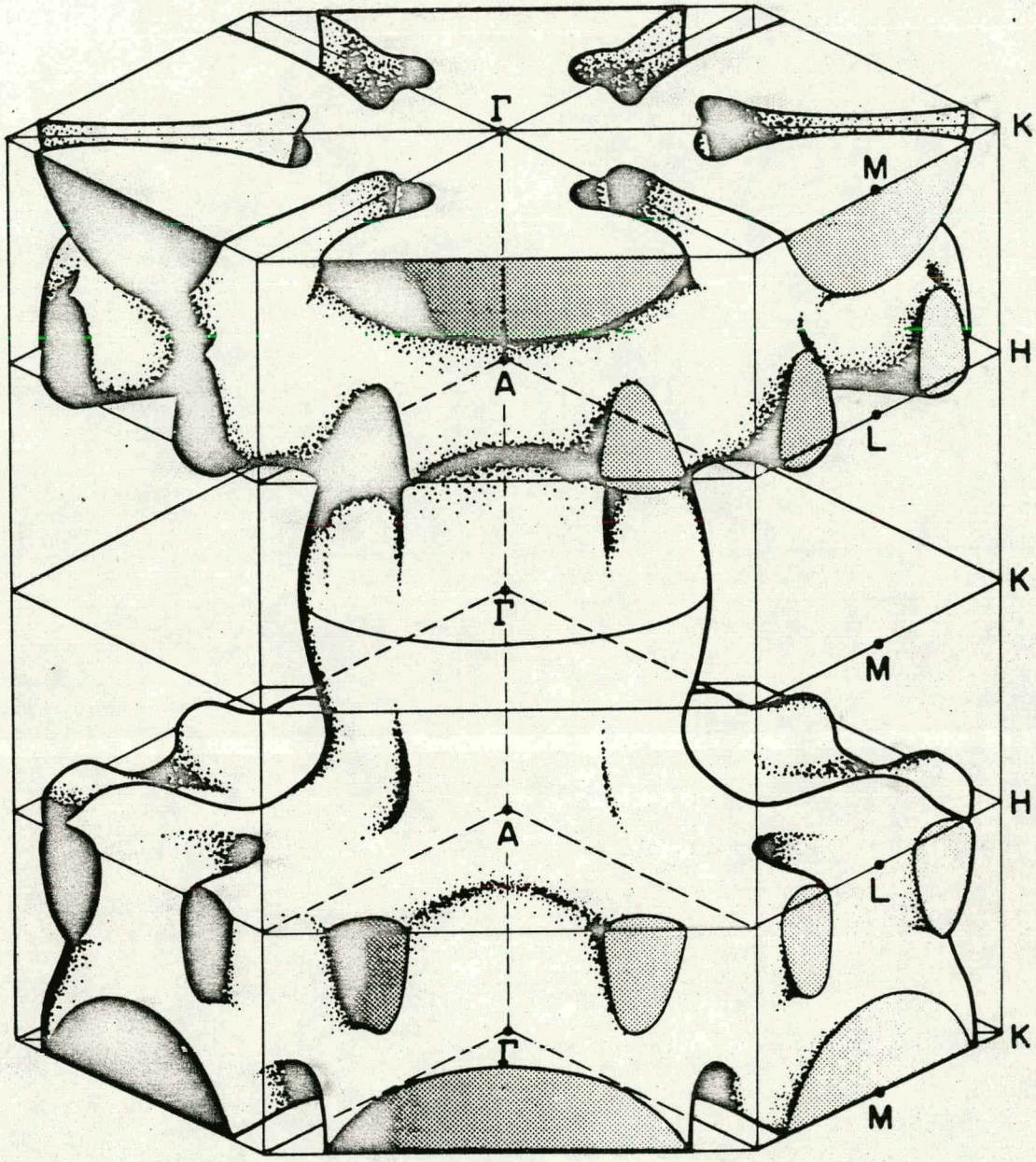

Figure 22. Fermi surface of gadolinium as calculated by Freeman et al. (64)

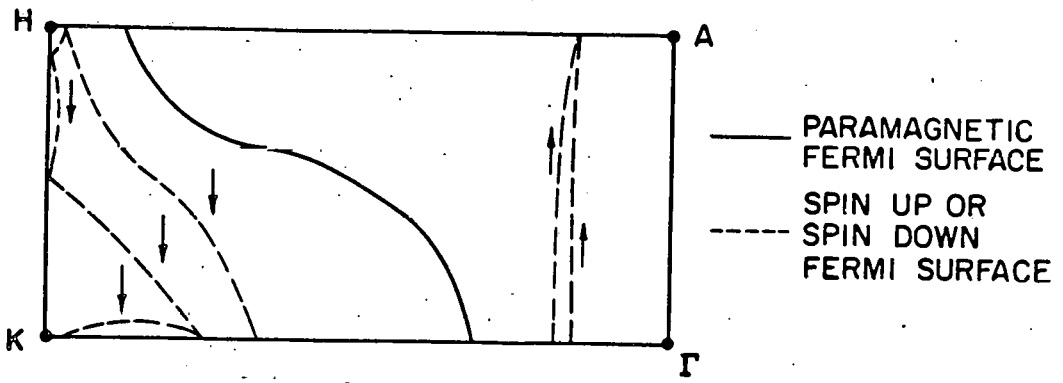

Figure 23a. This cross section of the gadolinium Fermi surface illustrates the distortion of the surface by exchange splitting below the Curie point

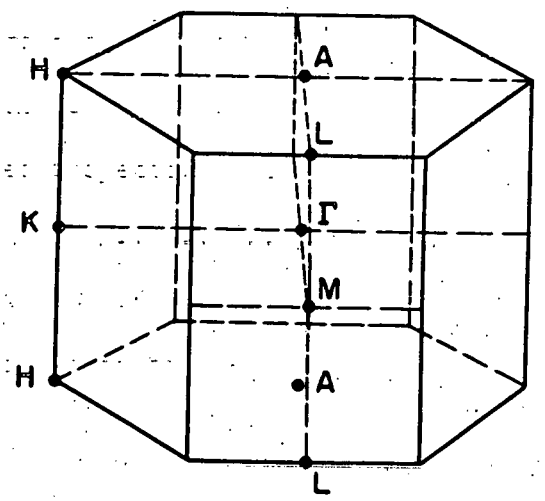

Figure 23b. Brillouin zone of the hexagonal close-packed structure

Figure 22 indicates that the Fermi surface of gadolinium is very anisotropic. The paramagnetic Fermi surfaces of the trivalent rare earths are rather similar. Loucks and Liu* recently estimated the anisotropy of the paramagnetic Fermi surface of erbium. Let A_a be the total area of the Fermi surface projected in the a-direction and A_c the total area of the Fermi surface projected in the c-direction. They found that for erbium

$$A_c/A_a = \int_{E_F} dS_c / \int_{E_F} dS_a = 2.1 \quad . \tag{5.1}$$

While the magnitude of this ratio may vary among the rare earths, it is very probable that high temperature anisotropy in the electrical resistivity is due to the anisotropy of the Fermi surface. The velocity factor in Equation 2.9a complicates the matter. Presumably, however,

$$\int_{E_F} V_c dS_c > \int_{E_F} V_a dS_a \tag{5.2}$$

still holds.

In the ferromagnetic region, Figure 23a indicates that the amount of surface area projected in the basal plane direction will be increased at the expense of area projected in the c-direction. Note, for example, that the two sheets of Fermi surface occupied by spin up electrons will contribute very little to the c-axis conductivity. Thus, the a-axis resistivity will decrease relative to the c-axis resistivity and the c-axis resistivity will increase relative to the a-axis resistivity. It has been shown experimentally that for gadolinium and terbium the electrical resistivities in

---

*T. L. Loucks and S. H. Liu, Physics Department, Iowa State University, Ames, Iowa. Private communication. 1968.

the two directions are more nearly equal in the ferromagnetic than in the paramagnetic region.

Some of the rare earths order antiferromagnetically. For example, Figure 8 illustrates the helical configuration in terbium and holmium. All the moments in a given plane of atoms are ordered ferromagnetically. However, the moments in adjacent planes are rotated through a fixed turn angle. Proceeding up the c-axis the moment configuration repeats itself after a given number of lattice spacings. The periodicity in the magnetic structure introduces planes of energy discontinuity in the electronic structure in a manner analogous to that in which the periodic arrangement of atoms in a crystal introduces Brillouin zone boundaries. The zone boundaries introduced by the magnetic periodicity are called super zones. Figure 24 shows cross sections of the Fermi surface of thulium as calculated by Freeman et al. (6). The light solid curves are the paramagnetic cross sections, the dark solid curves are the antiferromagnetic cross sections, and the horizontal lines are the superzone boundaries at $k_z = \pm n \times (2\pi/7c)$, where c is the lattice spacing in the c-direction. Figure 24 illustrates that in the helical state large sections of the Fermi surface whose normal is essentially parallel to the z-axis are wiped out, while sections whose normal is essentially perpendicular to the z-axis are perturbed but nearly unchanged. Loucks and Liu have also calculated for erbium the change in Fermi surface areas projected in various directions when superzones are introduced. They found that

$$\Delta A_c = 6\% \qquad \Delta A_a = 0.6\% \quad . \tag{5.3}$$

This change in the Fermi surface influences the conductivity integrals of Equations 2.9. In addition the c-axis conductivities can be expected to be

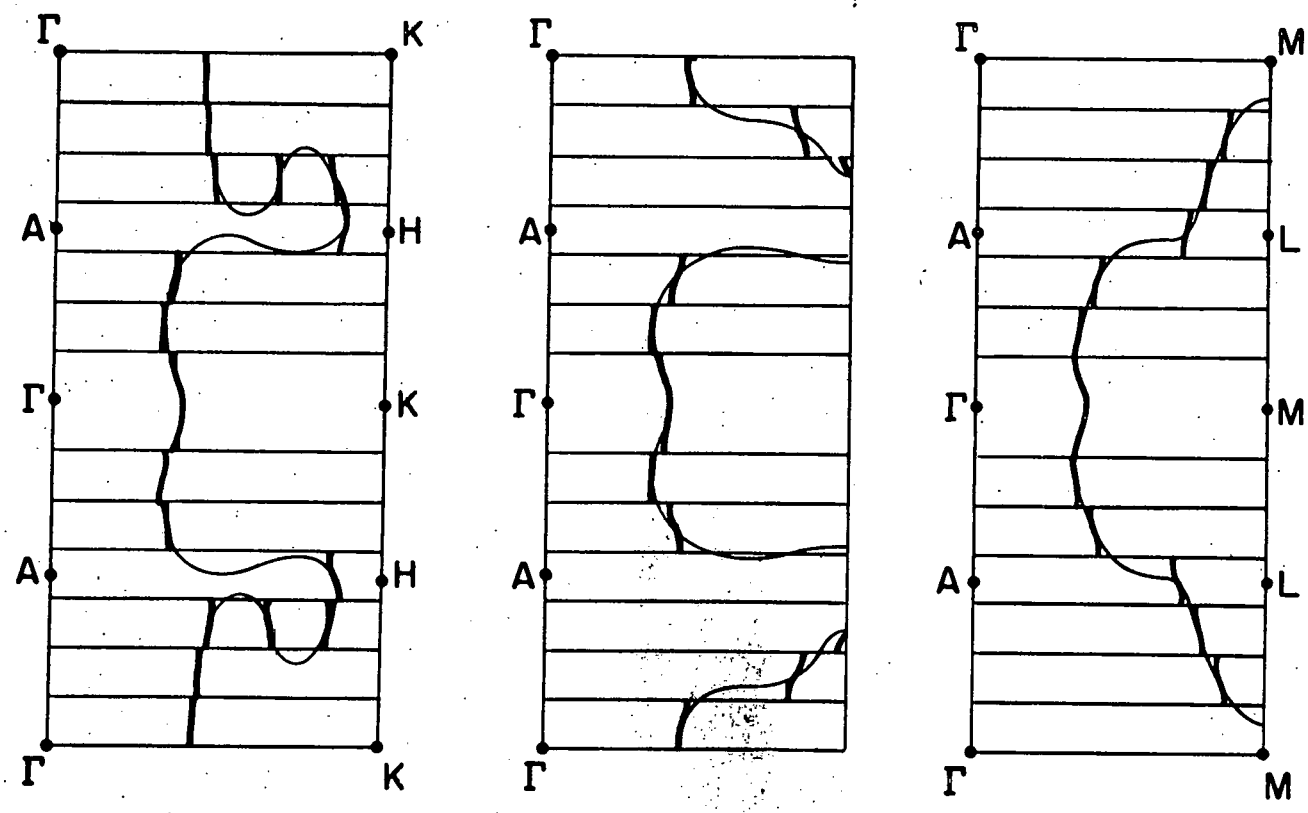

Figure 24. Some vertical cross sections of the thulium Fermi surface as calculated by Freeman et al. (6). The effect of the magnetic superzones (horizontal lines) is demonstrated by comparing the paramagnetic Fermi surface (light solid lines) and the antiferromagnetic Fermi surface (dark solid lines)

affected more than the basal plane conductivities.

The electrical resistivities of terbium and holmium as shown in Figures 16 and 17 show the effects of superzone boundaries. At T_c in terbium ρ_c increases sharply while ρ_a increases much less rapidly. The turn angle and energy gap are functions of temperature and this fact appears to affect ρ_c but not ρ_a. With increasing temperature the superzones are disappearing, the c-axis conductivity is increasing, and thus ρ_c starts to decrease. The over all effect is to cause a maximum below T_N in the c-axis resistivity curve. The disappearance of superzones and the fact that they affect c-axis conductivities much more than a-axis conductivities also explains the behavior of ρ_a and ρ_c in holmium below T_N. A free electron theory incorporating magnetic superzones was used by Elliott and Wedgewood (65) to explain the electrical resistivity of dysprosium, holmium, and erbium single crystals. Edwards (15) fitted his thulium resistivity data to this same theory. While the rare earths are not free electron-like, the theory does predict the higher slope in the basal plane resistivity and the maximum in the c-axis resistivity below the Néel temperature.

Above the magnetic ordering temperature the electrical resistivity can be represented by

$$\rho = \rho_o + \rho_s + \alpha T \quad , \tag{5.4}$$

where ρ_o is the residual resistivity, ρ_s is the spin disorder resistivity of Equation 2.15, and α is the slope of the high temperature resistivity. It is observed experimentally that $\rho_{sa} > \rho_{sc}$, $\alpha_a > \alpha_c$, and ρ_s is

considerably larger than ρ_o. If the impurity scattering is neglected, the relaxation time can be expressed as

$$\frac{1}{\tau} = \frac{1}{\tau_s} + \beta T \quad . \tag{5.5}$$

Substituting Equation 5.5 into Equation 2.9a,

$$\rho_a = (4\pi^3\hbar/e^2)\left(\int_{E_F} V_a dS_a\right)^{-1}(\beta T + \tau_s^{-1}) \quad , \tag{5.6a}$$

$$\rho_c = (4\pi^3\hbar/e^2)\left(\int_{E_F} V_c dS_c\right)^{-1}(\beta T + \tau_s^{-1}) \quad . \tag{5.6b}$$

These equations are of the form

$$\rho_a = \rho_{sa} + \alpha_a T \quad , \tag{5.7a}$$

$$\rho_c = \rho_{sc} + \alpha_c T \quad . \tag{5.7b}$$

Assuming that Equation 5.2 is valid and that β and τ_s are essentially isotropic, then

$$\rho_{sa}/\rho_{sc} = \alpha_a/\alpha_c = \int V_c dS_c / \int V_a dS_a > 1 \quad , \tag{5.8}$$

which is qualitatively in agreement with experiment. Data was not taken to high enough temperatures for the c-axis resistivity of gadolinium and terbium to fit Equation 5.4. The holmium data, however, was linear above 220°K, and for holmium

$$\rho_{sa}/\rho_{sc} = 1.88 \quad . \qquad \text{and} \qquad \alpha_a/\alpha_c = 1.60 \quad . \tag{5.9}$$

The discrepancy may be due to anisotropy in β and τ_s.

Electronic structure and electrical resistivity have been discussed prior to the thermal conductivity because electrical properties are simpler from the point of view of the number of carriers involved. Secondly,

electrons are a major carrier of heat and their properties seem to explain the thermal conductivity, at least qualitatively, near magnetic transitions.

At low temperatures electronic thermal conduction is impeded by impurity and phonon scattering. Equation 2.14 can be written as

$$T/K_e = A + BT^3 \quad . \tag{5.10}$$

A linear plot of T/K versus T^3 would indicate that this type of scattering is dominant. Figures 25, 26, and 27 show these plots for gadolinium, terbium, and holmium, respectively. The gadolinium data obeys this functional dependence quite well. While the terbium data and holmium data are more sparse, these elements also seem to obey this dependence over a slightly smaller temperature interval. Ideally, $A = \rho_o/L_o$, but as the figures indicate the actual situation is

$$A < \rho_o/L_o \quad . \tag{5.11}$$

The discrepancy may be due in part to the neglect of other carriers and scattering mechanisms, in particular, magnons.

The anisotropy of the thermal conductivity in the ferromagnetic region apparently has no explanation as can be offered for the electrical resistivity. K_c is always greater than K_a in terbium. In gadolinium there is a wide intermediate temperature range in which K_c is less than K_a. Boys' (12) results showed that in the ferromagnetic region of dysprosium, K_c is always less than K_a. The problem is compounded by the fact that there are three carriers. Two things, however, may in some way be responsible for the unusual anisotropy in gadolinium. First, the direction of the magnetization in gadolinium is a function of temperature. Thus, the band splitting may not only be a function of temperature but possibly of direction

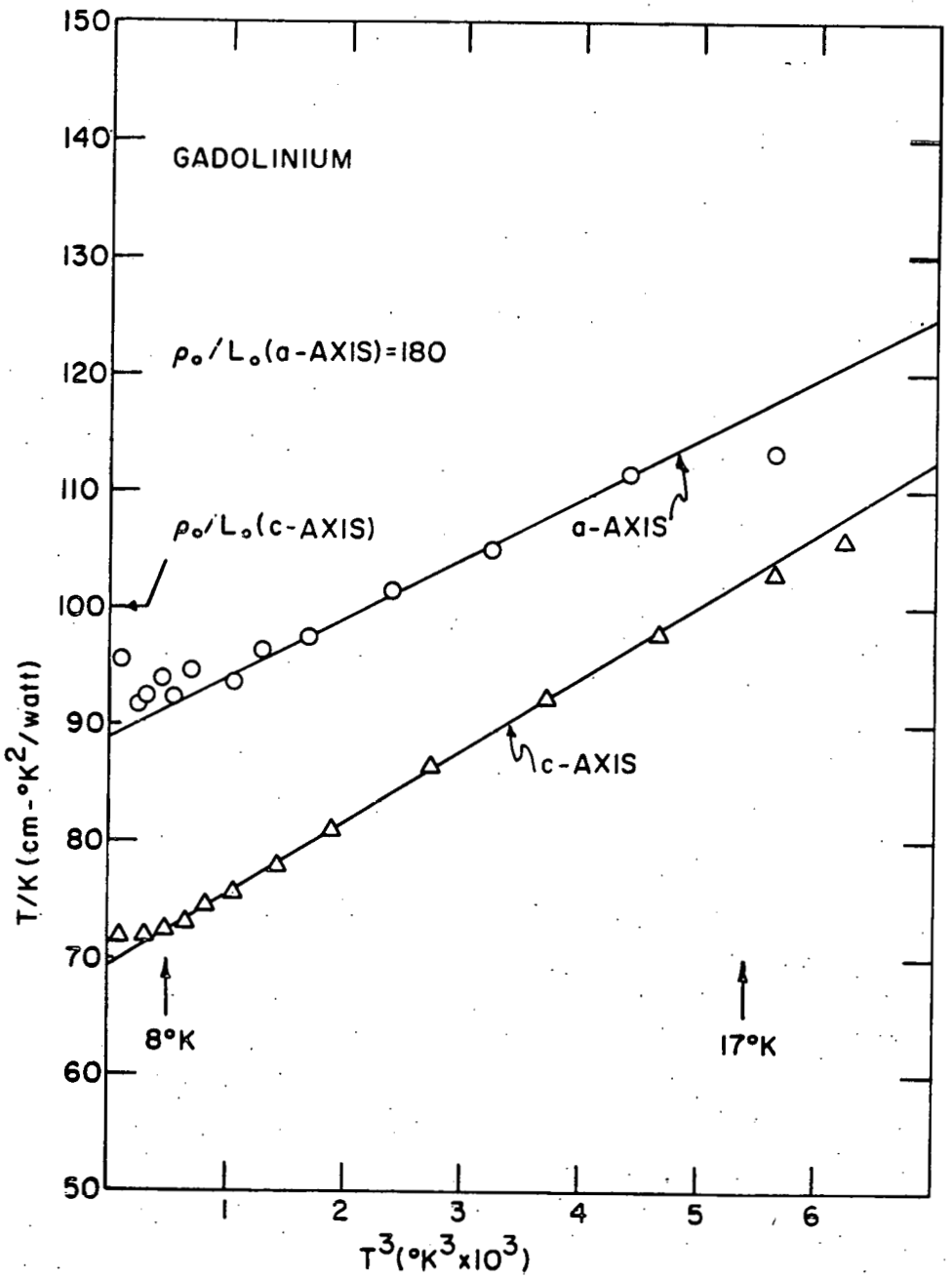

Figure 25. T/K versus T^3 for gadolinium

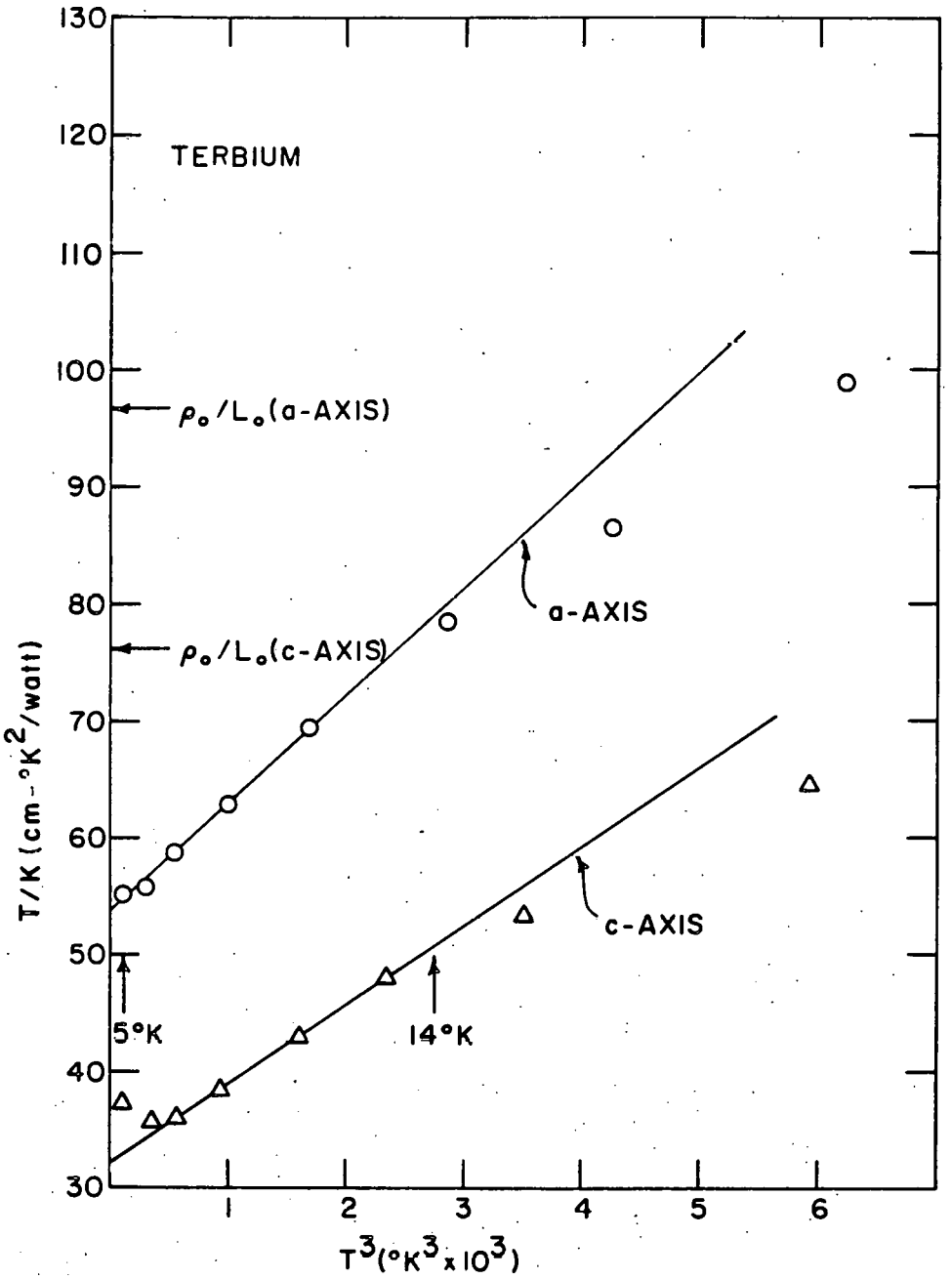

Figure 26. T/K versus T^3 for terbium

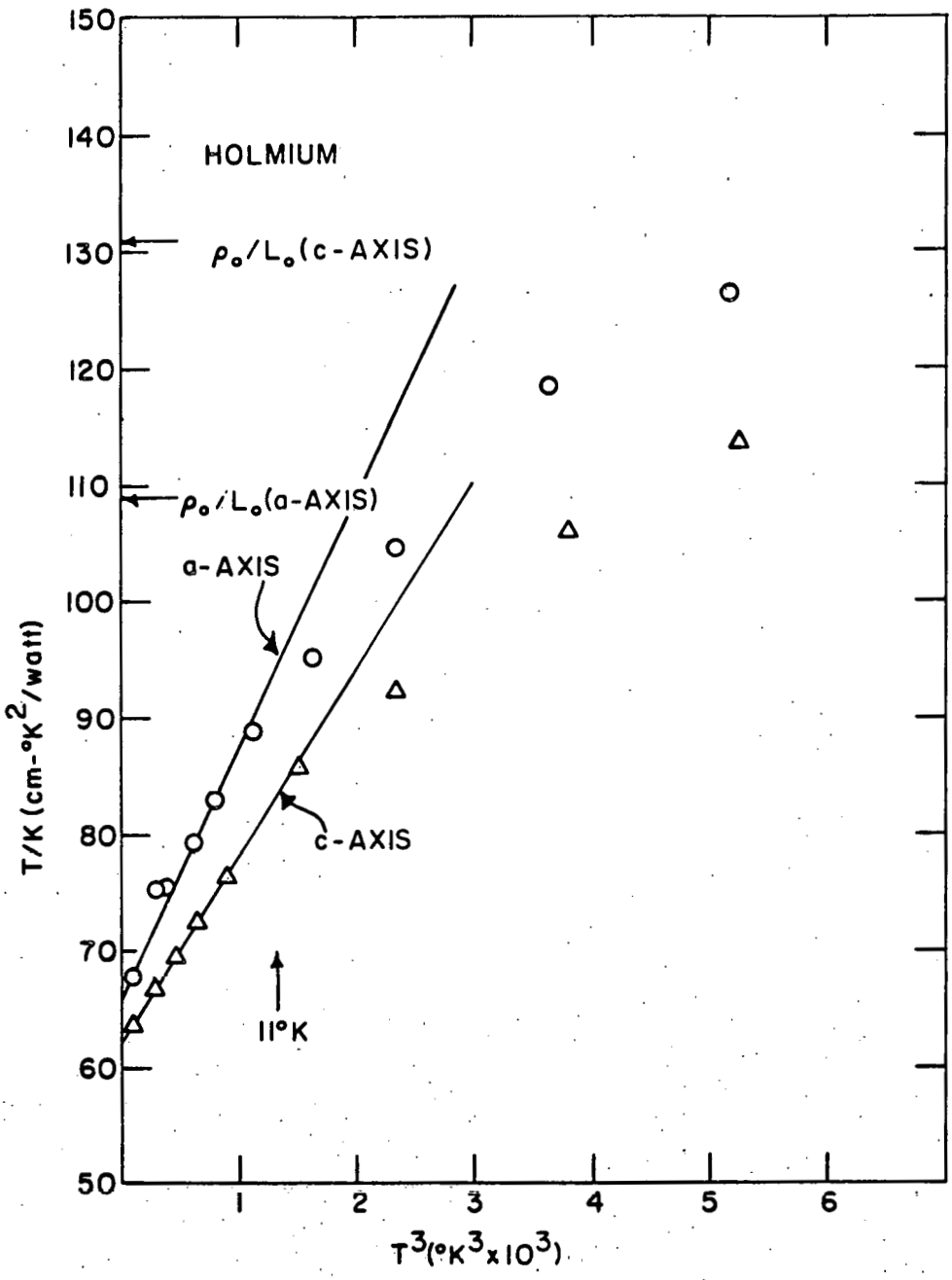

Figure 27. T/K versus T^3 for holmium

also. Secondly, Evenson and Liu (66) have recently shown that the Fermi surface of gadolinium is similar but distinctly different from those of dysprosium, erbium, and lutetium. The Fermi surface of gadolinium has slightly more surface area projected in the basal plane direction than do the Fermi surfaces for the other metals. This could account for an increase in K_a relative to K_c.

The effects on the thermal conductivity of the introduction of superzones in terbium and holmium at T_c are slight. In terbium ρ_c increased sharply at T_c, while K_c drops off slowly over an interval of ten degrees. ρ_a shows a pronounced change of slope, while K_a essentially shows no sign of T_c. In holmium K_c experiences only a 1% drop at 20^oK while erbium shows a sharp 25% drop (12) at the same temperature for a similar magnetic transition. This difference may be due to the fact that the c-axis component of magnetization in the conical ferromagnetic region in erbium is 8 Bohr magnetons, while in holmium it is only 2 Bohr magnetons. The change in magnetic structure in holmium at T_c is just not as great as it is in erbium.

The effect of superzones below T_N in holmium is apparent and correlates well with the electrical resistivity in the same region. K_a and K_c have approximately the same shape up to 100^oK. As the Neel point is approached the superzones are disappearing, the area of the Fermi surface projected in the c-direction is increasing, and K_c begins to increase as the temperature approaches T_N. K_c has a minimum at 111^oK, while ρ_c has a maximum at 117^oK. The superzones have only a slight effect on the a-axis conductivity. K_a keeps decreasing as the temperature approaches T_N.

The thermal conductivity increases above magnetic ordering

temperatures. This increase can be attributed to spin disorder scattering of the electrons by paramagnetic moments. Edwards and Legvold (67) have recently developed a fundamental explanation for the increase in thermal conductivity with increasing temperature. Assuming that at high temperature K_e can be separated from K by the Wiedemann-Franz law, consider the electronic thermal conductivity

$$K_e = L_o T/\rho \quad . \tag{5.12}$$

Combining this equation with Equation 5.4,

$$K_e = (L_o/\alpha)[1 + (\rho_o+\rho_s)/\alpha T]^{-1} \quad . \tag{5.13}$$

This equation says that as the temperature becomes very large K_e increases to the constant value L_o/α and that the rate of approach to that value depends on a characteristic temperature of value $(\rho_o+\rho_s)/\alpha$. In very pure non-magnetic materials $\rho_s=0$ and $\rho_o \simeq 0$, so that K_e is constant at high temperatures. Such behavior has been observed experimentally (62). Define

$$K_\infty = L_o/\alpha \quad , \tag{5.14a}$$

$$t = (\rho_o+\rho_s)/\alpha \quad . \tag{5.14b}$$

Then Equation 5.13 becomes

$$K_e = K_\infty [1+t/T]^{-1} \quad . \tag{5.15}$$

Table 2 indicates values of the thermal conductivity at 300°K, K_{300}, and values of K_∞ and t for samples whose high temperature resistivity could be described by Equation 5.4. ρ_s and α for the holmium a-axis I sample was assumed to be the same as that of the holmium a-axis II sample. Boys' results (12) were used to obtain the dysprosium and erbium values. Edwards' results (15) were used to obtain the thulium values.

Table 2. High temperature spin disorder thermal conductivity

Sample	K_{300} (watt/cm-^{o}K)	K_{∞} (watt/cm-^{o}K)	t(^{o}K)
Gd a-axis II	.103	.306	1390
Tb a-axis	.095	.204	713
Dy a-axis	.103	.178	456
Ho a-axis I	.125	.131	308
Ho a-axis II	.138	.131	241
Ho c-axis	.220	.209	221
Er b-axis	.128	.118	140
Er c-axis	.185	.227	141
Tm b-axis	.141	.116	118
Tm c-axis	.241	.206	88

A striking feature of Table 2 is the steady decrease in t from gadolinium through thulium. This decrease reflects the fact that ρ_s decreases and α increases from gadolinium through thulium. The high temperature data on erbium and thulium shows that the thermal conductivity levels off in the temperature range 2t-3t. If this range can be taken as a rule of thumb, it explains why the high temperature thermal conductivity of the other rare-earth metals listed has not leveled off by room temperature. For terbium, for example, K_a might not be expected to reach a constant value until about 1500°K.

Spin disorder scattering also seems to account for the fact that the two holmium samples of Figure 14 do not tend to have the same thermal conductivity near the Debye temperature. Before the two curves can come smoothly together, the Neel point is reached. Above the Néel point the conductivity begins to increase. The value of t for the relatively pure sample II is appreciably smaller than that of impure sample I. Equation 5.15, therefore, says that the conductivity of sample II will rise faster

and tend to level off sooner than will the conductivity of sample I. This behavior is evidenced in the two curves.

Extending electrical resistivity and thermal conductivity measurements to high temperatures might prove very fruitful. The spin disorder resistivity and high temperature slope for gadolinium, terbium, and dysprosium c-axis samples could then be determined. In addition since the phonon contribution to the thermal conductivity should be inversely proportional to temperature, perhaps the phonon portion can be made much smaller than the electronic contribution. In this event both the electrical resistivity and thermal conductivity would depend primarily on the electronic structure alone.

The final point to be discussed is the separation of the total thermal conductivity into its component parts. The simplest approach is to assume that the Wiedemann-Franz law is valid at high temperatures ($T > \theta_D$) and at low temperatures (in the residual resistance region). At these temperatures

$$K_g + K_m = K - L_o T/\rho \quad . \tag{5.16}$$

In the paramagnetic region $K_m=0$. Though speaking of non-magnetic materials, virtually all authors on the subject agree that this is a valid procedure at low temperatures (36,37,38,68,69,70). At high temperatures caution is often warned.

One generally accepted requirement for this procedure to be valid at high temperatures is that the metal be a relatively poor conductor. In this case electronic conduction should be sufficiently impeded so that phonon conduction can be appreciable. Wilson (68, p.295) says directly that an accurate separation can be expected in this situation. The rare

earths are relatively poor conductors. Mott and Jones (69, p.307) imply that if the Weidemann-Franz law applies and if $L > L_o$ the excess thermal conduction is due to phonons. Ziman (38, p.389) after investigating the electron-phonon interaction in some detail emphasizes the Weidemann-Franz law should hold precisely at high temperatures, independent of the shape of the Fermi surface and of the form of scattering matrix elements. This statement is encouraging in view of the extreme anisotropy of rare earth Fermi surfaces.

Klemens (36,70) has written extensively and critically on the separation of thermal conductivity into components due to various carriers. At high temperatures

$$K = K_e + K_g \quad , \tag{5.17a}$$

$$1/K_e = W_e = W_o + W_i \quad , \tag{5.17b}$$

where W_o is the residual thermal resistivity and W_i is the ideal thermal resistivity. Klemens points out that at high temperatures it may be difficult to separate the effects of K_g and W_i. However, he does say (36, p.260) that when L is appreciably larger than L_o, K_g can readily be determined by calculating K_e. Further he agrees (70, p.84) with the procedure of Powell and Tye (71) who separated the electron and phonon components of the thermal conductivity of chromium above room temperature by means of the Wiedemann-Franz law.

Table 3 lists K, K_e, and $K-K_e$ at 300^oK. K_e was calculated by means of the Wiedemann-Franz law. $K-K_e$ is very probably K_g.

Figure 28 shows a low temperature separation of the thermal conductivity of terbium.

Table 3. Components of K at 300°K. The units of K are watt/cm-°k.

Sample	K	K_e	$K-K_e$
Gd a-axis ll	0.103	0.053	0.050
Gd c-axis ll	0.108	0.062	0.046
Tb a-axis	0.0932	0.060	0.033
Tb c-axis	0.148	0.072	0.076
Ho a-axis ll	0.139	0.072	0.067
Ho c-axis	0.220	0.121	0.099

In short, when the Wiedemann-Franz law applies the fraction L_o/L of the thermal conductivity is the electronic contribution, while the remaining contribution is due to other carriers. The anomalously large values of L relative to L_o throughout the whole temperature range are most probably due to the fact that appreciable heat is conducted by carriers other than the electrons, namely, magnons and phonons.

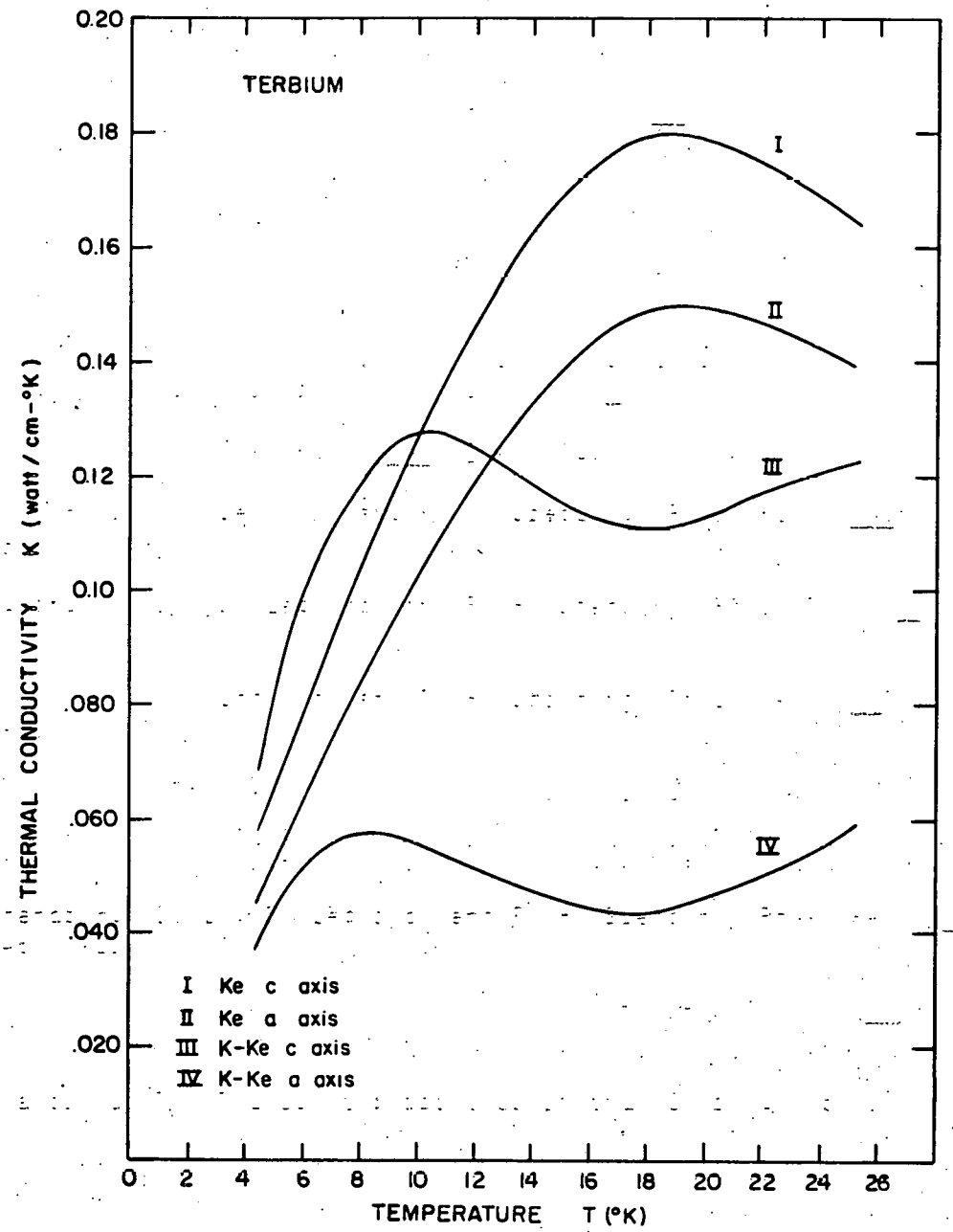

Figure 28. K_e and $K-K_e$ for the terbium a-axis and c-axis samples at low temperatures

VI. BIBLIOGRAPHY

1. Ruderman, M. A. and C. Kittel, Phys. Rev., 96, 99 (1954).

2. Liu, S. H., Phys. Rev., 121, 451 (1961).

3. Dimmock, J. O. and A. J. Freeman, Phys. Rev. Letters, 13, 750 (1964).

4. Keeton, S. C. and T. L. Loucks, Phys. Rev., 168, 672 (1968).

5. Williams, R. W., T. L. Loucks, and A. R. Mackintosh, Phys. Rev. Letters, 16, 168 (1966).

6. Freeman, A. J., J. O. Dimmock, and R. E. Watson, Phys. Rev. Letters, 16, 94 (1966).

7. Fleming, G. S. and T. L. Loucks, [Energy bands and Fermi surface of scandium, to be published in Phys. Rev., ca. 1968].

8. Loucks, T. L., Phys. Rev., 144, 504 (1966).

9. Nigh, H. E., S. Legvold, and F. H. Spedding, Phys. Rev., 132, 1092 (1963).

10. Hegland, D. E., S. Legvold, and F. H. Spedding, Phys. Rev., 131, 158 (1963).

11. Hall, P. M., S. Legvold, and F. H. Spedding, Phys. Rev., 117, 971 (1960).

12. Boys, D. W., Thermal conductivity of dysprosium, erbium, and lutetium single crystals, unpublished Ph.D. thesis, Ames, Iowa, Library, Iowa State University of Science and Technology, 1967.

13. Strandburg, D. L., S. Legvold, and F. H. Spedding, Phys. Rev., 127, 2046 (1962).

14. Green, R. W., S. Legvold, and F. H. Spedding, Phys. Rev., 122, 827 (1961).

15. Edwards, L. R., Transport properties of thulium single crystals, unpublished Ph.D. thesis, Ames, Iowa, Library, Iowa State University of Science and Technology, 1967.

16. Sill, L. R. and S. Legvold, Phys. Rev., 137, A1139 (1965).

17. Edwards, L. R. and S. Legvold, Thermoelectric power of lutetium single crystals, unpublished data, Ames, Iowa, Department of Physics, Iowa State University of Science and Technology, ca. 1967.

18. Lee R. S. and S. Legvold, Phys. Rev., 162, 431 (1967).

19. Rhyne, J. J., [Anomalous hall effect in single-crystal dysprosium, to be published in Phys. Rev., ca. 1968].

20. Liu, S. H., D. R. Behrendt, S. Legvold, and R. H. Good, Jr., Phys. Rev., 116, 1464 (1959).

21. Richards, D. B., The high field magnetization of thulium single crystals, unpublished Ph.D. thesis, Ames, Iowa, Library, Iowa State University of Science and Technology, 1968.

22. Legvold, S. and F. H. Spedding, U.S. Atomic Energy Commission Report ISC-508 [Ames Lab., Ames, Iowa], 11 (1954).

23. Arajs, S. and R. V. Colvin, J. Appl. Phys., 35, 1043 (1964).

24. Arajs, S. and R. V. Colvin, Phys. Rev., 136, A439 (1964).

25. Colvin, R. V. and S. Arajs, Phys. Rev., 133, A1076 (1964).

26. Arajs, S. and G. R. Dunmyre, Physica, 31, 1466 (1965).

27. Powell, R. W. and B. W. Jolliffe, Phys. Letters, 14, 171 (1965).

28. Aliev, N. G. and N. V. Volkenshtein, SovietPhys. - JETP, 22, 17 (1966).

29. Aliev, N. G. and N. V. Volkenshtein, Soviet Phys. - Solid State, 7, 2068 (1966).

30. Aliev, N. G. and N. V. Volkenshtein, Soviet Phys. - JETP, 22, 997 (1966).

31. Jolliffe, B. W., R. P. Tye, and R. W. Powell, J. Less-Common Metals, 11, 388 (1966).

32. Karagyozyan, A. G. and K. V. Rao, Physics Letters, 25A, 235 (1967).

33. Karagyozyan, A. G. and K. V. Rao, [A study of anisotropy effects in thermal conductivity of terbium, to be published in Soviet Physics - JETP, ca. 1968].

34. Rao, K. V., Physics Letters, 24A, 39 (1967).

35. Nikolskii, G. S. and V. V. Eremenko, Phys. Stat. Sol., 18, K123 (1966).

36. Klemens, P. G., Handbuch der Physik, 14, 198 (1956).

37. Mendelssohn, K. and H. M. Rosenberg, Solid State Phys., 12, 223 (1961).

38. Ziman, J. M., Electrons and phonons, London, England, Oxford University Press, 1960.

39. Schriempf, J. T., Phys. Rev. Letters, 20, 1034 (1968).

40. Dekker, A. J., J. Appl. Phys., 36, 906 (1965).

41. Liu, S. H. and D. B. Siano, Phys. Rev., 164, 697 (1967).

42. Peierls, R., Ann. Phys., Ser. 5, 3, 1055 (1929).

43. Kawasaki, K., Prog. Theor. Phys., 29, 801 (1963).

44. Stern, H., J. Phys. Chem. Solids, 26, 153 (1965).

45. Sato, H., Progr. Theoret. Phys. (Kyoto), 13, 119 (1955).

46. Douthett, D. and S. A. Friedberg, Phys. Rev., 121, 1662 (1961).

47. Lüthi, B., J. Phys. Chem. Solids, 23, 35 (1962).

48. Douglass, R. L., Phys. Rev., 129, 1132 (1963).

49. McCollum, D. C., R. L. Wild, and J. Callaway, Phys. Rev., 136, A426 (1964).

50. Bhandari, C. M. and G. S. Verma, Phys. Rev., 152, 731 (1966).

51. Spedding, F. H. and J. E. Powell, J. Metals, 6, 1131 (1954).

52. Nigh, H. E., J. Appl. Phys., 34, 3323 (1963).

53. Sill, L. R., Seebeck effect in heavy rare earth single crystals, unpublished Ph.D. thesis, Ames, Iowa, Library, Iowa State University of Science and Technology, 1964.

54. Rhyne, J. J., Magnetostriction of dysprosium, erbium, and terbium single crystals, unpublished Ph.D. thesis, Ames, Iowa, Library, Iowa State University of Science and Technology, 1965.

55. Powell, R. L., M. D. Bunch, and R. J. Corruccini, Cryogenics, 1, 139 (1961).

56. Dauphinee, T. M., Can. J. Phys., 31, 577 (1953).

57. Norén, B. and O. Beckman, Ark. Fysik, 25, 567 (1964).

58. Colvin, R. V., S. Legvold, and F. H. Spedding, Phys. Rev., 120, 741 (1960).

59. Cable, J. W. and E. O. Wollan, Phys. Rev., 165, 733 (1968).

60. Koehler, W. C., H. R. Child, E. O. Wollan, and J. W. Cable, J. Appl. Phys., 34, 1335 (1963).

61. Koehler, W. C., J. W. Cable, E. O. Wollan, and M. K. Wilkinson, J. Phys. Soc. Japan, 17, Suppl. B-3, 32 (1962).

62. White, G. K. and S. B. Woods, Phil. Trans. R. Soc. Ser. A, 251, 273 (1959).

63. Boas, W. and J. K. Mackenzie, Prog. Metal Phys., 2, 90 (1950).

64. Freeman, A. J., J. O. Dimmock and R. E. Watson, [The augmented plane wave method and the electronic properties of rare earth metals, to be published in Löwdin, P. O., ed., ca. 1967].

65. Elliott, R. J. and F. A. Wedgewood, Proc. Phys. Soc., 81, 846 (1963).

66. Evenson, W. E. and S. H. Liu, Phys. Rev. Letters, 21, 432 (1968).

67. Edwards, L. R. and S. Legvold, [Transport properties of thulium single crystals, to be published in Phys. Rev., ca. 1968].

68. Wilson, A. H., The theory of metals, 2nd ed., Cambridge England, Cambridge University Press, 1965.

69. Mott, N. F. and H. Jones, The theory of the properties of metals and alloys, New York, New York, Dover Publications, Inc., 1958.

70. Klemens, P. G., Solid State Phys., 7, 1 (1958).

71. Powell, R. W. and R. P. Tye, J. Inst. Metals, 85, 185 (1956).

VII. ACKNOWLEDGEMENTS

The author would like to thank his major professor, Dr. Sam Legvold, for his advice, encouragement, and general interest in the well-being of his students.

Thanks are extended to Dr. B. C. Carlson for the interest and encouragement he has shown the author throughout his graduate career.

The author wishes to express his gratitude to Dr. S. H. Liu for many valuable discussions and in particular for his help in constructing Figure 23 of this work. Appreciation is expressed to Dr. D. K. Finnemore and Dr. C. A. Swenson for many informative conversations. The author wishes to express his gratitude to Mr. B. J. Beaudry for providing the arc-melted rare earth buttons.

Sincere thanks must go to Dr. D. W. Boys and Dr. L. R. Edwards for stimulating an interest in and teaching the techniques of transport property measurement.

Thanks are extended to Dr. D. B. Richards, Dr. R. S. Lee, Mr. C. M. Cornforth, Mr. D. W. Mellon, Mr. J. L. Broderick, and Mr. A. R. Harvey for numerous interesting conversations. Special thanks must go to Mr. D. W. Mellon for the loan of his equipment for resistivity measurements.

The author wishes to express his appreciation to Mr. Bill Sylvester and to Mr. Russ Clark for constructing some of the equipment, to Mr. Paul Ness and Mr. Mike Sandholm for providing liquid hydrogen to meet the author's sporadic needs, to Mr. Frank Witter for taking much of the resistivity data, to Mr. Gary Erskine for helping to maintain equipment and process data, and to Mr. Carl Kingsbury for his nocturnal assistance.

The author wishes to especially thank his wife, Carole, for her encouragement and for typing the rough draft.

VIII. APPENDIX

A. Sample Impurities

Residual resistivity and the resistance ratio ($\rho_{300}/\rho_{4.2}$) are indicative of sample purity. Table 4 lists these two values for the samples used in this investigation. The residual resistivities are in units of $\mu\Omega$-cm.

Table 4. Residual resistivities and resistance ratios

Sample	Residual Resistivity	Resistance Ratio
Gd a-axis II	4.43	31.4
Gd c-axis II	2.62	46.8
Gd c-axis I	2.7[a]	45[a]
Tb a-axis	2.37	52.1
Tb c-axis	1.87	54.5
Ho a-axis I	15.24	7.1
Ho a-axis II	2.67	37.8
Ho c-axis	3.21	18.9

[a]This sample was used by Sill and these are the values quoted by him (53).

Table 5 is a listing of sample purities. Gaseous impurities were determined by vacuum fusion analysis; the other impurities were determined by semi-quantitative analysis. Impurities are recorded in ppm by weight. Both gadolinium II samples came from the same button, and the analysis listed is for these samples. Both terbium samples came from the same button. All holmium samples came from the same production batch. The gadolinium and terbium were analyzed after the single crystals were grown. The holmium analysis was made prior to crystal growth. The analysis of the gadolinium c-axis I samples is recorded by Sill (53).

Table 5. Sample impurities

Impurities	Gd	Tb	Ho
Al	< 20	30	< 30
Ca	< 30	60	< 20
Co	-	-	
Cr	< 10	300	< 20
Cu	< 20	100	
Dy	< 200	< 100	< 200
Er	-	-	< 500
Fe	20	< 50	< 40
Gd		< 200	
H	5	5	2
Ho	< 500	-	
Mg	20	< 10	10
Mn	-	-	
Mo	-	-	
N	13	3	
Ni	< 20	< 20	< 60
O	218	160	48
Sc	-	-	
Si	< 30	< 20	< 40
Sm	< 100	T	
Ta	< 200	< 200	
Tb	< 500		
Tm	-	-	< 200
W	< 500	500	
Yb	FT	FT	< 50

Symbols: T=trace, FT=faint trace. A blank space means that the element was not investigated.

B. Sample Dimensions

Sample dimensions are listed in Table 6. All values are the sample size for the thermal conductivity measurements. Samples often needed to be

polished before they could then be inserted into the electrical resistivity apparatus. Consequently, the sample dimensions for the electrical resistivity measurements are all smaller than the values listed in Table 6.

Table 6. Sample dimensions

Sample	Height (cm)	Width (cm)	Length (cm)
Gd a-axis II	0.201	0.233	1.223
Gd c-axis II	0.186	0.214	0.831
Gd c-axis I	0.107	0.113	1.702
Tb a-axis	0.228	0.232	2.207
Tb c-axis	0.184	0.231	0.885
Ho a-axis I	0.194	0.204	1.087
Ho a-axis II	0.238	0.239	0.701
Ho c-axis	0.181	0.189	0.659

C. Tabulation of Thermal Conductivity Data

The thermal conductivities are in units of watt/cm-^{o}K and the temperatures are in ^{o}K.

Table 7. Thermal conductivity of Gd a-axis II crystal

T	K	T	K	T	K
4.8	.0502	14.8	.141	33.2	.180
6.3	.0688	16.4	.147	37.2	.180
6.9	.0746	17.8	.157	42.3	.176
7.7	.0820	19.5	.166	47.2	.175
8.2	.0888	22.2	.172	53.2	.171
8.9	.0941	22.4	.170	60.0	.168
10.2	.109	23.8	.174	68.4	.164
10.9	.113	26.1	.177	76.6	.161
11.9	.122	28.1	.182	90.7	.153
13.4	.132	30.0	.180	79.7	.158

Table 7 (Continued)

T	K	T	K	T	K
88.7	.154	237.8	.110	293.3	.101
100.0	.148	250.0	.107	295.2	.101
114.7	.143	260.1	.106	297.7	.103
129.8	.138	269.9	.104	300.0	.103
144.9	.134	275.1	.103	302.7	.104
160.0	.129	280.0	.103	305.9	.105
175.0	.126	282.9	.102	309.9	.106
190.8	.121	285.9	.102	315.2	.108
208.0	.117	289.0	.102	320.1	.110
223.1	.113	291.8	.101	329.8	.113

Table 8. Thermal conductivity of Gd c-axis ll crystal

T	K	T	K	T	K
4.7	.0654	29.4	.167	205.2	.112
6.9	.0961	32.8	.163	220.1	.110
7.9	.109	35.5	.161	235.3	.107
8.7	.119	40.4	.158	250.0	.105
9.4	.126	45.2	.155	259.9	.105
10.2	.135	52.1	.152	270.0	.105
11.3	.145	60.1	.148	273.0	.104
12.4	.153	67.8	.145	277.9	.104
14.0	.162	75.9	.142	282.7	.104
15.5	.168	90.1	.136	285.9	.105
16.7	.171	86.8	.138	288.9	.106
17.8	.173	99.9	.131	292.0	.106
18.4	.174	115.0	.127	293.7	.106
19.6	.177	130.4	.125	295.6	.107
20.5	.175	144.6	.122	298.1	.108
23.3	.173	160.1	.118	300.9	.108
24.8	.172	175.0	.116	305.0	.109
27.3	.170	190.2	.113	310.1	.110

Table 9. Thermal conductivity of Gd c-axis I crystal

T	K	T	K	T	K
4.8	.0762	26.0	.220	65.8	.174
6.7	.108	21.3	.215	75.4	.165
7.9	.126	23.0	.222	89.4	.158
9.8	.149	25.0	.223	87.8	.151
11.9	.167	27.1	.215	100.0	.145
13.9	.181	29.9	.212	115.3	.137
15.7	.191	32.7	.201	130.0	.131
17.6	.198	37.9	.201	144.8	.126
19.2	.206	42.6	.193	159.9	.119
20.6	.209	50.2	.186	174.8	.115
22.8	.219	57.8	.181		

Table 10. Thermal conductivity of Tb a-axis crystal

T	K	T	K	T	K
4.7	.0852	73.9	.141	215.5	.0848
6.7	.120	81.5	.136	218.1	.0854
8.1	.138	91.4	.130	220.7	.0829
10.0	.159	92.3	.129	222.5	.0832
11.9	.171	103.8	.123	224.9	.0823
14.2	.181	115.6	.118	227.7	.0812
16.2	.187	131.8	.111	229.3	.0809
18.4	.186	147.8	.106	231.1	.0800
21.0	.191	154.1	.104	233.4	.0807
24.1	.198	162.7	.102	236.6	.0819
21.5	.198	170.3	.0979	240.1	.0820
24.7	.200	177.6	.0976	244.9	.0832
28.0	.194	184.6	.0938	249.9	.0841
31.7	.189	191.0	.0918	260.7	.0870
39.2	.175	200.1	.0893	270.1	.0880
44.9	.163	205.0	.0887	285.0	.0917
52.2	.157	209.8	.0854	300.3	.0932
59.3	.151	213.4	.0866	309.3	.0980
66.5	.145				

Table 11. Thermal conductivity of Tb c-axis crystal

T	K	T	K	T	K
4.8	.129	65.7	.201	220.0	.125
7.1	.199	73.4	.196	221.2	.124
8.3	.230	85.9	.187	222.5	.123
9.8	.255	99.4	.179	224.6	.123
11.7	.272	89.7	.182	226.7	.123
13.3	.277	103.0	.174	228.7	.124
15.2	.285	117.6	.168	230.1	.124
18.1	.280	132.4	.158	231.6	.126
21.3	.293	148.9	.152	234.7	.127
23.2	.293	165.5	.145	237.5	.127
26.6	.280	179.9	.139	240.5	.130
31.0	.257	195.1	.133	244.4	.130
35.4	.242	200.0	.132	250.6	.132
38.9	.236	204.9	.129	257.9	.135
39.3	.234	210.0	.129	271.6	.141
44.5	.221	213.8	.128	285.9	.144
51.1	.213	216.6	.127	298.9	.148
58.4	.207	218.7	.126		

Table 12. Thermal conductivity of Ho a-axis ll crystal

T	K	T	K	T	K
4.7	.0691	17.3	.137	33.9	.146
6.7	.0889	18.6	.141	38.5	.146
7.3	.0966	19.7	.142	44.7	.149
7.9	.103	20.8	.140	52.6	.152
8.5	.107	21.7	.141	60.3	.151
9.3	.112	22.4	.138	68.6	.147
10.4	.117	23.5	.136	76.4	.143
11.8	.124	25.1	.137	85.9	.135
13.3	.127	27.3	.141	94.0	.129
15.4	.130	30.4	.142	103.7	.125

Table 12. (Continued)

T	K	T	K	T	K
113.6	.120	132.8	.114	195.9	.125
118.8	.117	135.4	.114	210.8	.128
123.7	.115	138.9	.114	225.7	.131
126.5	.114	142.8	.115	240.0	.133
128.8	.114	147.9	.117	255.7	.134
130.2	.114	155.9	.117	270.4	.135
130.6	.113	165.8	.119	285.9	.137
131.3	.113	180.7	.122	298.7	.139

Table 13. Thermal conductivity of Ho c-axis crystal

T	K	T	K	T	K
4.7	.0738	29.7	.166	131.5	.168
6.8	.102	32.6	.170	132.1	.169
7.8	.112	37.7	.176	133.6	.170
8.7	.120	43.5	.180	135.7	.172
9.7	.127	50.4	.182	138.8	.173
11.5	.134	58.6	.181	140.8	.175
13.3	.144	66.8	.179	143.7	.176
15.6	.147	74.8	.173	149.9	.179
16.6	.151	85.0	.168	160.6	.184
17.4	.153	89.6	.162	175.6	.191
18.0	.156	101.1	.156	190.5	.195
18.5	.159	110.7	.154	205.8	.202
19.7	.159	115.7	.155	220.7	.206
19.9	.156	120.7	.159	235.7	.209
20.8	.156	123.4	.161	250.6	.211
21.8	.156	126.8	.161	266.5	.214
23.0	.157	129.4	.165	282.9	.217
24.5	.158	130.4	.166	298.7	.222
26.8	.162				

Table 14. Thermal conductivity of Ho a-axis I crystal

T	K	T	K	T	K
4.7	.0232	23.2	.0902	123.4	.0980
6.7	.0305	25.5	.0963	126.5	.0977
7.9	.0359	27.3	.0984	129.0	.0983
8.6	.0382	30.9	.103	130.8	.0992
9.2	.0403	33.4	.104	133.1	.0987
10.3	.0449	36.3	.103	135.7	.0994
10.8	.0466	39.9	.107	138.4	.100
11.4	.0486	42.6	.107	142.5	.101
12.4	.0520	45.9	.110	148.0	.102
14.0	.0577	50.3	.111	158.1	.104
15.4	.0634	56.5	.112	170.1	.107
16.0	.0663	63.5	.115	185.3	.109
17.2	.0685	70.6	.114	200.0	.111
18.2	.0722	77.6	.112	215.0	.112
19.4	.0772	84.7	.108	230.0	.114
20.2	.0794	91.7	.106	244.9	.116
20.8	.0799	88.2	.106	260.3	.119
21.5	.0847	97.5	.103	274.9	.122
22.5	.0896	108.3	.102	186.9	.123
24.5	.0967	113.5	.0995	299.0	.126
21.5	.0861	118.7	.0979		

D. Tabulation of Electrical Resistivity Data

The electrical resistivities are in units of $\mu\Omega$-cm and the temperatures are in ^{o}K.

Table 15. Electrical resistivity of Gd a-axis II crystal

T	ρ	T	ρ	T	ρ
4.3	4.45	5.9	4.46	10.1	4.53
5.0	4.46	7.9	4.48	12.0	4.62

Table 15. (Continued)

T	ρ	T	ρ	T	ρ
14.1	4.75	144.7	70.31	304.9	139.65
16.0	4.93	159.6	78.17	310.0	140.14
18.0	5.17	174.8	86.15	315.0	140.61
20.1	5.47	189.7	93.97	328.2	141.88
22.0	5.88	205.0	102.04	196.3	97.35
20.2	5.52	220.0	110.43	198.0	98.31
23.0	6.09	234.9	117.45	199.9	99.28
25.9	6.79	250.0	123.53	201.9	100.35
29.8	8.17	260.0	127.26	203.6	101.28
34.5	9.89	269.9	130.75	205.8	102.44
39.8	12.17	274.9	132.44	207.8	103.55
47.8	16.13	280.0	134.08	209.8	104.61
55.8	20.54	284.0	135.38	212.1	105.88
63.8	25.14	287.0	136.33	213.9	106.89
71.9	29.89	289.9	137.29	216.0	108.06
79.9	34.61	292.0	138.05	218.0	109.22
77.4	33.12	293.1	138.30	219.6	110.15
85.7	38.00	293.9	138.42	221.9	111.44
100.0	46.14	296.0	138.70	223.6	112.43
113.9	53.88	299.0	139.03	225.8	113.39
129.6	62.30	302.0	139.33	228.3	114.53

Table 16. Electrical resistivity of Gd c-axis ll crystal

T	ρ	T	ρ	T	ρ
4.2	2.62	18.0	3.50	40.0	9.31
5.9	2.68	20.1	3.79	47.8	12.40
8.8	2.76	20.4	3.76	55.9	15.80
10.1	2.82	23.1	4.34	63.9	19.41
12.0	2.93	26.0	4.93	72.1	23.20
14.1	3.08	29.9	6.04	83.1	28.37
16.0	3.27	34.8	7.54	77.2	24.86

Table 16. (Continued)

T	ρ	T	ρ	T	ρ
88.3	30.70	219.9	100.20	289.9	123.45
100.3	36.57	235.2	107.60	291.9	123.42
114.7	43.76	250.0	113.80	292.9	123.33
129.6	51.44	259.7	117.23	293.9	123.23
145.2	59.63	269.9	120.22	295.9	123.03
159.9	67.64	275.1	121.40	299.1	122.75
175.0	75.91	279.8	122.28	303.9	122.32
190.1	84.21	283.9	122.89	310.0	121.79
204.8	92.21	287.0	123.23		

Table 17. Electrical resistivity of Tb a-axis crystal

T	ρ	T	ρ	T	ρ
4.2	2.367	57.0	17.44	218.3	105.52
4.6	2.369	65.6	21.70	220.3	107.86
5.9	2.372	75.0	26.48	222.3	109.47
8.1	2.386	90.5	34.35	224.3	110.68
9.9	2.418	87.7	32.94	226.5	112.02
12.0	2.476	98.9	38.74	228.8	113.30
14.0	2.581	113.5	46.42	230.5	114.04
16.0	2.734	129.5	55.11	233.5	114.67
18.1	2.957	146.0	64.36	237.4	115.31
20.1	3.257	160.6	72.72	240.0	115.78
20.8	3.384	173.6	80.19	246.2	116.59
20.3	3.300	187.5	88.14	252.3	117.39
23.7	3.951	198.5	94.48	261.6	118.56
28.3	5.111	204.9	98.00	276.9	120.51
34.9	7.436	209.7	100.65	288.0	121.92
41.3	10.04	213.7	102.87	298.0	123.16
49.0	13.54	216.1	104.28		

Table 18. Electrical resistivity of Tb c-axis crystal

T	ρ	T	ρ	T	ρ
4.2	1.873	83.6	28.20	231.5	102.68
4.9	1.877	95.1	33.82	233.9	102.11
5.9	1.881	109.7	41.21	237.1	101.70
8.0	1.896	124.5	49.14	239.2	101.46
10.0	1.931	139.8	57.68	242.8	101.13
12.0	1.992	155.3	66.88	247.0	100.81
14.0	2.103	168.6	75.01	250.1	100.72
16.0	2.253	185.2	84.49	254.7	100.60
17.9	2.447	194.6	89.13	261.2	100.56
20.1	2.738	199.6	91.73	265.6	100.60
22.0	3.064	205.0	94.46	271.6	100.72
20.3	2.776	210.3	96.86	278.4	100.85
22.8	3.212	213.3	98.04	285.4	101.05
27.2	4.185	216.3	99.18	293.1	101.46
32.8	5.847	218.5	99.91	299.4	101.98
40.8	8.770	220.3	103.16	214.5	98.32
47.6	11.52	222.6	104.30	219.0	99.83
55.6	15.00	225.3	104.75	219.3	100.03
64.0	18.86	226.9	104.47	219.7	100.81
72.3	22.74	229.1	103.29	220.0	102.23

Table 19. Electrical resistivity of Ho a-axis ll crystal

T	ρ	T	ρ	T	ρ
4.6	2.78	19.0	5.79	24.0	7.79
6.2	2.85	20.0	6.25	27.1	9.22
8.0	2.99	21.0	6.65	30.1	10.42
9.9	3.25	22.0	7.01	34.7	12.43
11.9	3.61	23.8	7.71	40.2	14.93
14.1	4.16	20.2	6.32	47.9	18.67
15.9	4.69	21.0	6.66	55.5	22.57
17.9	5.33	21.9	7.00	64.4	27.46

Table 19. (Continued)

T	ρ	T	ρ	T	ρ
72.1	31.95	124.7	65.83	160.1	74.03
79.8	36.75	127.8	67.25	175.0	77.03
90.0	43.48	129.8	67.90	189.9	80.06
77.3	35.06	130.8	68.08	204.7	83.01
89.8	43.38	132.0	68.29	219.7	85.97
99.4	49.81	134.4	68.83	239.6	89.81
109.7	56.55	136.7	69.28	259.7	93.64
114.6	59.75	139.9	69.93	279.7	97.36
118.7	62.33	144.5	70.85	299.6	100.97
121.9	64.27	149.7	71.90		

Table 20. Electrical resistivity of Ho c-axis crystal

T	ρ	T	ρ	T	ρ
5.1	3.207	29.4	11.58	130.3	46.38
6.0	3.280	34.8	13.82	131.2	45.49
7.7	3.477	41.0	16.58	132.1	45.44
10.0	3.852	48.4	20.03	134.1	45.24
12.0	4.319	56.7	24.17	137.3	45.13
13.8	4.852	64.3	28.17	140.5	45.14
15.8	5.522	71.7	32.44	144.9	45.24
17.9	6.252	89.1	42.79	149.8	45.45
19.0	6.975	77.8	35.51	159.7	46.05
20.1	7.609	86.4	41.05	174.4	47.17
21.0	7.967	95.3	46.01	189.5	48.54
21.7	8.255	102.4	49.27	204.4	49.98
24.1	9.161	109.3	51.47	219.7	51.62
20.2	7.696	114.4	52.34	239.4	53.73
21.0	8.103	119.9	52.27	259.0	56.10
21.8	8.397	122.1	51.87	279.6	58.55
23.8	9.155	124.8	50.93	297.7	60.58
27.0	10.58	127.8	49.14		

Table 21. Electrical resistivity of Ho a-axis I crystal

T	ρ	T	ρ	T	ρ
4.2	15.24	19.0	18.47	26.1	21.32
4.9	15.32	20.0	18.86	28.9	22.47
5.9	15.38	21.0	19.28	31.9	23.71
7.5	15.53	22.1	20.01	35.3	25.21
9.0	15.74	23.0	20.34	42.7	28.75
10.4	16.00	24.0	20.75	50.7	32.94
12.1	16.39	20.4	19.19	59.2	37.45
14.2	16.98	21.3	19.49	67.9	42.45
16.0	17.52	21.7	19.63	77.2	47.79
18.2	18.20	23.6	20.36	295.1	108.4

E. Discussion of Errors

The thermal conductivity, K, is computed from

$$K = (L/A)(\dot{Q}/\Delta T) \quad . \tag{8.1}$$

The fractional error in K is

$$\delta K/K = [(\delta L/L)^2 + (\delta A/A)^2 + (\delta\dot{Q}/\dot{Q})^2 + (\delta(\Delta T)/\Delta T)^2]^{1/2} \quad . \tag{8.2}$$

The last two terms in the brackets determine the relative error while all the terms in the bracket contribute to the absolute error.

The length, L, of the sample was measured to within 1%. The cross sectional area, A, was measured to within 2-4%. Thus, the geometrical factor, L/A, is known to an accuracy of about 4%.

The power flowing through the sample is computed from

$$\dot{Q} = P - \Delta P \quad , \tag{8.3}$$

where P is the measured power into the gradient heater and ΔP is the power lost through radiation and through conduction up lead wires. P could be

measured to within 0.5%. ΔP is negligible below $60^{\circ}K$ and appreciable above $150^{\circ}K$. The radiation losses are accurate to about 2-4% above $100^{\circ}K$. Thus, at low temperatures $\dot{Q}$ is known to about 1%, while at high temperatures it is known to about 4%.

It is interesting to note that the fractional errors in L/A and $\dot{Q}$ are indirectly related. A short sample, for example, might have a large uncertainty in its L/A value. However, a large amount of power would be necessary to establish a gradient across the sample and even at room temperature P could be much larger than ΔP. Thus, $\dot{Q}$ would be known quite accurately.

The temperature difference, ΔT, is computed from

$$\Delta T = E_{corr}/\text{Sensitivity}, \tag{8.4}$$

where

$$E_{corr} = E_{meas} + \Delta E \quad , \tag{8.5}$$

$$\text{Sensitivity} = dE/dT \quad . \tag{8.6}$$

E_{meas} is the measured output of the comparator, ΔE is the zero temperature difference correction, and E(T) is the EMF generated by the thermocouple at temperature T. The fractional error in ΔT is about 2%.

Summing up the errors by means of Equation 8.2 the absolute error in K is estimated to be 5-6%.

The resistivity, ρ, is computed from

$$\rho = (A/L)(V/I) \quad . \tag{8.7}$$

The fractional error in ρ is

$$\delta\rho/\rho = [(\delta A/A)^2 + (\delta L/L)^2 + (\delta V/V)^2 + (\delta I/I)^2]^{1/2} \quad . \tag{8.8}$$

Again, the fractional error in A/L is about 4%. The fractional error in the voltage, V, is about 0.5% at low temperatures and about 0.025% at

high temperatures. The fractional error in the current is about 0.05%. Thus, the relative error in ρ ranges from 0.1-0.5%. The absolute error in ρ is estimated to be 4%.